

Response to Reviewer1

This paper sets out a methodology and presents summary results for assimilating aerosol index measurements in to an aerosol forecasting model. This is relevant and interesting for the modelling community as it is effectively aerosol radiance assimilation. Radiance assimilation is common place in the NWP data assimilation community but has still to be explored for aerosol assimilation. For NWP it provides improved results compared to a level 2 retrieval and it has not yet been established whether the same may be true for aerosol assimilation. The article is very nicely written and provides a clear and precise overview of the work carried out. The detail of the forward model and assimilation procedure used is thoroughly covered but the clear structure of the article means the overall message of the paper is not lost in all the detail. The results of the assimilation experiment are succinctly presented in easy to understand figures without inflating the results or claiming more than is shown. This well written paper presents an advance to modelling science and deserves publication. I do, however, have a few minor comments that I list below

We thank the reviewer for his/her constructive comments

Minor comments

Question 1. It was not quite clear to me from the article whether the three models whose results are compared were the same version of the NAAPS model? I understand that the NAAPS reanalysis v1 was used to show the results with AOD assimilation (pg 8, paragraph 1) and that a free running version was used to provide the results without any aerosol assimilation at all (line 176). You also state that the assimilation system is based on variations of aerosol particles from NAAPS (line 106). Are all three the same version at the same resolution or are there differences between them? It would be beneficial to clarify this in the article as any differences will also impact on the results of the three experiments compared to Aeronet.

Response: *The same research version of the NAAPS model is used for all three experiments. For the natural runs, only the NAAPS forecast model was used, that is, without any form of data assimilation. For the NAAPS reanalysis version 1, NAAPS was run with additional assimilation using MODIS and MISR AOD data. For the OMI AI data assimilation as presented in the study, NAAPS was run with the newly developed OMI AI assimilation. All three runs are at the same spatial and temporal resolutions, and are driven by the same meteorology and model physics. We expect that differences among three model runs resulted from the different aerosol data assimilation schemes implemented versus the natural run. We have added the following sentence to clarify the issue:*

“Note that the same version of the NAAPS model with the same temporal and spatial resolutions, and driven by the same meteorological data, were used in constructing Figure 5 and thus the differences in Figures 5a, 5b and 5c only result from different aerosol data assimilation methods implemented (no data assimilation for the natural run).“

Question 2. Related to this, I'm slightly confused by your description of the post-processing system in lines 209-211. I would consider the construction of a new NAAPS analysis based on the background NAAPS aerosol concentrations and increments as derived from the assimilation system to be part of the assimilation process itself. In fact I would assume that this updated analysis state would be forecast forward in time to create the background state for the next cycle of the data assimilation process. Is this not the case?

Response: *Post-processing as mentioned in lines 209-211 is a part of the typical data assimilation process. In a typical data assimilation method, increments are constructed based on the differences between observations and modeled parameters (innovations), as well as error characteristics of both model and observations. These increments include new changes that need to be made for each model grid. At the last step of a typical data assimilation process, the modeled background is updated by adding those increments (or corrections) to construct a revised background state (analysis). The revised background state is then used as the initial state for the forecast for the next time cycle.*

In another word, analysis = background + increments. Note that a similar post-processing step is also included in the NAVDAS-AOD for MODIS and MISR AOD assimilation (Zhang et al., 2008).

Zhang, J. and J. S. Reid, D. Westphal, N. Baker, and E. Hyer, A System for Operational Aerosol Optical Depth Data Assimilation over Global Oceans, J. Geophys. Res., 113, D10208, doi:10.1029/2007JD009065, 2008.

Question: 3. Your Figure 7 is a comparison of the vertical profiles of the NAAPS natural and AI DA runs. Assuming that the AI DA runs are as described above, so an analysis model state that is used as the initial condition for a short forecast to create the background state for the next assimilation cycle, then I don't believe you can draw the conclusions that you do in lines 493-498. There is no guarantee that the profile before assimilation is the same as the nature run profile and so you can not disentangle what profile differences come from previous assimilation versus what is due to the assimilation of the AI data in the current cycle. To look at the impact of assimilating AI data in one specific cycle you would need to plot the background model state versus the analysis state, rather than the nature run.

Response: *Both natural and OMI AI DA runs were performed with the same version of the NAAPS model, at the same spatial and temporal resolutions, with the same initial conditions at the beginning of the study period (00Z, July 1, 2007). The only difference between the two-month natural and OMI AI DA runs is that OMI AI data assimilation was implanted in the OMI AI DA run, while OMI AI data assimilation was not implanted for the natural run. Therefore, the differences between the two model runs arise uniquely from the OM AI data assimilation process.*

Note that for a given cycle, once the model has begun integrating forward in time, the differences in vertical profiles between the natural and OMI AI DA runs will also be impacted by increments from previous cycles (after the starting date of the study period). So the differences between

OMI DA and natural runs as shown in Figure 7 can be considered as an integrated effect of OMI AI DA from 00Z, July 01 to 12 Z, July 28, 2007.

We added the following sentence to avoid confusion: “Note that the differences between OMI DA and natural runs as shown in Figure 7 are essentially an integrated effect of OMI AI DA from 00Z, July 01 to 12 Z, July 28, 2007.”

Question 4. What do you think is the impact of using gridded OMI data (line 130-133) versus the higher resolution (I assume) AOD data of the reanalysis. Do you think that the results would change if you were able to use the AI data at its native resolution and that it would closer match the results of the reanalysis?

***Response :** I assume the reviewer meant to say “high resolution (I assume) AI data” based on the second sentence. Changes are definitely expected with the use of AI at its native resolution. This is because each data point included/removed will introduce changes in the computed increments. Still, for a given grid, the gridded OMI data represents the averaged properties for that grid. Thus, we expect the difference between using gridded data or OMI data at the native resolution to be marginal.*

Question 5. It is interesting and useful to have an idea of the computational burden of the call to the radiative transfer model in Section 4.4, but it would add perspective if this could be compared to the equivalent computational burden for AOD assimilation.

Response: The time scale for running AOD assimilation for 1 month is at the hourly level, depending on the machines used. We have added the following remark:

“In comparison, the time scale for running AOD assimilation for 1 month is at the hourly level.”

Typos

Question: Pg. 7, line 147: AERONET

***Response:** done.*

Question: Pg. 8, line 169: precipitation data are used to constrain the wet removal process

***Response:** done*

Question: Pg. 18, line 405-407: It is unclear to me which figures you are talking about in this sentence. I assume it is Figure 3c, but coming directly after discussion of a comparison of 3b to 3d it needs further clarification.

Response: *We added Figure 3c in the text.*

Responses to reviewer 2 comments

This paper develops a data assimilation scheme using the VLIDORT radiative transfer model and simulated aerosol information from the NAAPS model to assimilate OMI AI measurements into the NAAPS model. Including the OMI AI assimilation improves the NAAPS simulation compared to the OMI AI, and improves NAAPS simulated AOD compared to AERONET AOD, but it does not outperform the NAAPS reanalysis AOD compared to AERONET. Overall the paper is well written and their data assimilation approach is well explained. I do have some comments.

We thank the reviewer for his/her comments

Question : My main issue with the paper is that the authors state in the abstract: “Improvements in model simulations demonstrate the utility of OMI AI data assimilation for improving the accuracy of aerosol model analysis over cloudy regions and bright surfaces.” But this is not really shown anywhere in the paper.. On line 149 it is even stated: “As AERONET data require a cloud-free line of sight to the solar disk, the performance of OMI AI data assimilation over overcast regions is not evaluated.” Yes there are AI measurements over cloudy regions and bright surfaces, but nowhere in the paper have the authors specifically evaluated the performance of their analysis over bright or cloudy surfaces compared to, say, the NAAPS reanalysis AOD from MODIS and MISR. The authors even state that their assimilation does not improve the NAAPS AOD compared to the reanalysis AOD, so where is the evidence of improvement over bright and cloudy surfaces? It is not explicitly stated which products from MODIS and MISR go into the NAAPS reanalysis, but both MODIS deep blue and MISR retrieve AOD quite accurately over bright surfaces, especially deserts, so this statement really should be backed up somehow.

Response: *One of the advantages of OMI AI is its ability to detect UV- absorbing aerosols over cloudy skies as well bright surfaces such as over desert regions and snow/ice-covered regions. In this study, we examined the possibility of assimilating OMI AI data over cloudy regions as well as desert regions (bright surfaces). All quality-checked (excluding noisy data and data with row anomalies) OMI AI data over cloudy regions and desert regions were used in the assimilation process. In comparison, no reliable AOD retrievals are available over cloudy regions from traditional passive-based aerosol retrieval methods. Also, retrievals over the desert regions are also limited to select algorithms. Therefore, having the OMI AI data assimilation capability over cloudy regions and over bright surfaces is an advancement in aerosol data assimilation.*

We agree with the reviewer that it is hard to evaluate NAAPS performance over cloudy regions. We also agree that OMI AI is an indirect indicator of aerosol properties, and assimilating OMI AI typically cannot out-perform assimilating of MODIS/MISR AOD over cloud free regions. Nonetheless, the improvements in NAAPS analyses over cloudy regions or bright surfaces through OMI AI DA can be directly or indirectly illustrated from three aspects.

First, our study suggests, based on the AERONET evaluation, that over cloud-free regions, in comparing NAAPS natural runs (without aerosol assimilation), the accuracy of NAAPS analyses is improved with the assimilation of OMI AI data. This suggests OMI AI data can be used to improve NAAPS performance. Also, OMI AI has comparable capability to detect UV absorbing aerosols over cloud-free skies as well over cloudy skies, thus, benefits in NAAPS analysis over cloudy regions or bright surfaces are expected through assimilating quality-controlled OMI AI data over cloudy and bright surfaces. Note, no passive-based AOD data are currently available for assimilation over cloudy regions.

Secondly, as the reviewer mentioned, there are AI measurements over cloudy regions and bright regions for evaluation. We have performed this approach in the paper. One of the steps for a data assimilation system is to check the difference between observation and analysis (O-A), as well as the difference between observation and background (O-B). OMI AI can be considered as observations. NAAPS data includes aerosol concentrations, and thus to perform O-A or O-B, we used the forward model and computed simulated OMI AI using NAAPS data. The two-month (July and August 2007) mean O-A is shown in Figure 4d and the two-month mean O-B is shown in Figure 4h. While near zero O-A values are found for the study region as shown in Figure 4d, large O-B values can be found in Figure 4h over heavy smoke and dust aerosol polluted regions. Note to compute two-month mean O-A and O-B, both NAAPS and OMI AI data over both cloudy and cloud-free skies were used. At the instantaneous level, Figures 3b and 3f show the O and A for 12UTC, July 28, 2007. Figures 3b and 3e show the O and B for 12 UTC, July 28, 2007 as well. Again, while observation and simulated AI using NAAPS analysis are similar over both cloudy regions and cloud free regions, large discrepancies can be found between OMI AI and simulated OMI AI using NAAPS natural run data. The O-A/O-B analyses at both two-month mean and instantaneous levels indicating NAAPS performance can be improved over cloudy regions.

Third, as a qualitative check, as highlighted in red ellipses in Figure 3, the NAAPS AOD patterns after OMI AI DA show a very similar spatial pattern to OMI AI over both cloudy and non-cloudy regions. This can be considered as an indirect indicator that NAAPS AOD patterns match OMI AI patterns after OMI AI DA, even over cloudy regions.

However, we have revised the sentence along the lines suggested by the reviewer: "Improvements in model simulations demonstrate the utility of OMI AI data assimilation for aerosol model analysis over cloudy regions and bright surfaces"

Other comments:

Question: - In section 4.3 Sensitivity Analysis, the authors discuss how varying smoke SSA affects the AI and conclude that there is a need for regionally varying SSA values for smoke to be included for future studies. However, the issue is not necessarily varying smoke SSA, it is the fact that the model used in this paper treats all "smoke" as one aerosol type with a single SSA value. In reality, "smoke" is composed of both black and organic (that is, brown) carbon, which have different SSA values, and different areas have different contributions of black and brown carbon to the overall "smoke". So really what the authors are showing is a major limitation in modelling absorbing aerosol with the particular model they chose.

Response: *Agreed. However, the problem we are encountering is very similar to that faced by the passive-based AOD retrieval community. Dust/smoke aerosol properties vary as a function of region and season, creating a problem not only for this study but for AOD retrievals using passive sensors. To deal with this problem, regional-based aerosol properties are used in some algorithms (e.g MODIS Dark Target). Similar methods may be also adopted for this study, as we have mentioned. However, this is outside the scope of our paper and is the subject for a future study.*

Question:- Also in section 4.3, the authors state: “Interestingly, although simulated AI values are significantly affected by perturbing SSA values as shown in Figure 6, less significant impacts are observed for NAAPS AOD.” However, this is to be expected, because AOD is a measure of the total extinction due to the presence of aerosols, so changing the fraction that is either scattering or absorbing would not change the overall extinction.

Response: *NAAPS-modeled UV-absorbing aerosol (dust and smoke) concentrations are corrected based on OMI AI observations. We agree that dust and smoke aerosols are only a fraction of the total aerosol concentration.*

Question: - Lines 136-139: “Isolated high AI values are removed as follows. First, for a 4x4 pixel box, if the mean AI is less than 0.7 but an individual AI value is larger than 0.7, then that one value is removed. Second, if the standard deviation of AI values for a 3x3 pixel box surrounding a pixel is larger than 0.5, that individual AI value is likewise removed” It is not explained how the authors came up with this criteria, and it might be helpful for them to include a bit of an explanation.

Response: *Both approaches are essentially homogeneity tests that are used for identifying outliers. The thresholds are estimated empirically through visual inspection.*

We added this sentence: “Note that both approaches are essentially homogeneity tests that are used for identifying outliers. The thresholds are estimated empirically through visual inspection.”

Technical comments:

Question: - Lines 80-86 are worded a little confusingly: “AI retrievals are currently computed using observations from sensors with ozone-sensitive channels. For example, the Ozone Monitoring Instrument (OMI), Ozone Mapping and Profiler Suite (OMPS), TROPospheric Monitoring Instrument (TROPOMI) and the future Plankton, Aerosol, Cloud and ocean Ecosystem (PACE) mission can detect UV-absorbing aerosol particles, such as black carbon laden smoke or iron-bearing dust, over bright surfaces, such as desert, snow and ice covered

regions, and aerosol plumes above clouds (e.g. Torres et al., 2012; Yu et al., 2012; Alfaro-Contreras et al., 2014; 2016).” At first it is being discussed how AI retrievals use ozone sensitive channels, then the “for example” is talking about detecting absorbing aerosols.

Response: *We revised the sentence to read: “For example, the Ozone Monitoring Instrument (OMI), Ozone Mapping and Profiler Suite (OMPS), TROPospheric Monitoring Instrument (TROPOMI) and the future Plankton, Aerosol, Cloud and ocean Ecosystem (PACE) mission include ozone-sensitive channels that can detect UV-absorbing aerosol particles, such as black carbon laden smoke or iron-bearing dust, over bright surfaces, such as desert, snow and ice covered regions, and aerosol plumes above clouds (e.g. Torres et al., 2012; Yu et al., 2012; Alfaro-Contreras et al., 2014; 2016).”*

Question: - Line 276: dust “plums” should be “plumes”

Response: *Done.*

Question: - Line 453: “proving” should be “providing”

Response: *Done.*

Response to short comment

We thank the executive editor for the comment. We will add the version number in the revised version of the paper as suggested.

The OMI data assimilation scheme (V1.0) is constructed using VLIDORT and NAVDAS-AOD for NAAPS analyses and forecasts. The VLIDORT radiative transfer code is a property of RT Solutions Inc. The distribution of the full VLIDORT package is publicly available, and comes with a standard GNU public license, through direct contact with RT Solutions Inc. (http://www.rtslidort.com/mainprod_vlidort.html). Both NAAPS and NAVDAS-AOD are proprietary to the Naval Research Laboratory, United States Department of the Navy. Given their association with a defense system, they are not available publicly. This situation is similar to that in other major centers such as ECMWF, JMA, and UKMO. Nevertheless, both NAAPS and NAVDAS-AOD are well documented in past studies (e.g. Lynch et al., 2016; Zhang et al., 2008; 2011; 2014; Rubin et al., 2017) and we have made every effort to thoroughly report our methods so that they may be replicated. In addition, AOD fields from the NAAPS OMI AI DA runs and natural runs over the study region and for the study period will be shared in the supplement.

We have revised the code and data availability section to read:

Code and data availability: The OMI data assimilation scheme (V1.0) is constructed using VLIDORT and NAVDAS-AOD for NAAPS analyses and forecasts. The VLIDORT radiative transfer mode is a property of RT Solutions Inc. The VLIDORT code is publicly available, and comes with a standard GNU public license, through direct contact with RT Solutions Inc. (http://www.rtslidort.com/mainprod_vlidort.html). Both NAAPS and NAVDAS-AOD are proprietary to Naval Research Laboratory, United States Department of the Navy. Nevertheless, both NAAPS and NAVDAS-AOD are well documented in past studies (e.g. Lynch et al., 2016; Zhang et al., 2008; 2011; 2014; Rubin et al., 2017) and we have made every effort to thoroughly report our methods so that they may be replicated. AOD fields from the NAAPS OMI AI DA and natural runs over the study region and period are shared as the supplement to the paper for readers who are interested. The NAAPS reanalysis data are available from the USGODAE web site (https://nrlgodae1.nrlmry.navy.mil/cgi-bin/datalist.pl?dset=nrl_naaps_reanalysis&summary=Go). The OMI OMAERUV data are available from the NASA's Goddard Earth Sciences Data and Information Services Center (*GES DISC*; https://disc.gsfc.nasa.gov/datasets/OMAERUV_003/summary). AERONET data are obtained from the NASA AERONET webpage (<https://aeronet.gsfc.nasa.gov/>).

1
2
3
4
5
6
7
8
9
10
11
12
13
14
15
16
17
18
19
20
21
22
23
24
25

Development of an OMI AI data assimilation scheme for aerosol modeling over bright surfaces—a step toward direct radiance assimilation in the UV spectrum

Jianglong Zhang¹, Robert J. D. Spurr², Jeffrey S. Reid³, Peng Xian³, Peter R. Colarco⁴, James R. Campbell³, Edward J. Hyer³, and Nancy Baker³

¹Department of Atmospheric Sciences, University of North Dakota, Grand Forks, ND

²RT SOLUTIONS Inc., Cambridge MA

³Marine Meteorology Division, Naval Research Laboratory, Monterey, CA

⁴NASA Goddard Space Flight Center, Greenbelt, MD

Revised version sSubmitted to

GMD

September~~June~~ 2020

Corresponding Author: jianglong.zhang@und.edu

26 **Abstract**

27 Using the Vector Linearized Discrete Ordinate Radiative Transfer (VLIDORT) code as the main
28 driver for forward model simulations, a first-of-its-kind data assimilation scheme has been
29 developed for assimilating Ozone Monitoring Instrument (OMI) aerosol index (AI) measurements
30 into the Naval Aerosol Analysis and Predictive System (NAAPS). This study suggests both RMSE
31 and absolute errors can be significantly reduced in NAAPS analyses with the use of OMI AI data
32 assimilation, when compared to values from NAAPS natural runs. Improvements in model
33 simulations demonstrate the utility of OMI AI data assimilation for ~~r~~ ~~improving the accuracy of~~
34 aerosol model analysis over cloudy regions and bright surfaces. However, the OMI AI data
35 assimilation alone does not out-perform aerosol data assimilation that uses passive-based aerosol
36 optical depth (AOD) products over cloud free skies and dark surfaces. Further, as AI assimilation
37 requires the deployment of a fully-multiple-scatter-aware radiative transfer model in the forward
38 simulations, computational burden is an issue. Nevertheless, the newly-developed modeling
39 system contains the necessary ingredients for assimilation of radiances in the ultra-violet (UV)
40 spectrum, and our study shows the potential of direct radiance assimilation at both UV and visible
41 spectrums, possibly coupled with AOD assimilation, for aerosol applications in the future.
42 Additional data streams can be added, including data from TROPOspheric Monitoring Instrument
43 (TROPOMI), Ozone Mapping and Profiler Suite (OMPS) and eventually with the Plankton,
44 Aerosol, Cloud and ocean Ecosystem (PACE) mission.

45

46

47 **1.0 Introduction**

48 Operational chemical transport modeling (CTM) of atmospheric aerosol particles,
49 including simulation of sources and sinks and long-range transport of aerosol events such as
50 biomass burning aerosols from fires and dust outbreaks, is now commonplace at global
51 meteorology centers for air quality and visibility forecasts (e.g. Sessions et al, 2015; Lynch et al.,
52 2016). Variational and ensemble-based assimilation of satellite derived aerosol products such as
53 aerosol optical depth (AOD), lidar backscatter measurements, and surface aerosol properties, can
54 substantially improve accuracies in CTM analyses and forecasts (Zhang et al., 2008; 2011; 2014;
55 Yumimoto et al., 2008; Uno et al., 2008; Benedetti et al., 2009; Schutgens et al., 2010; Sekiyama
56 et al., 2010; Saide et al. 2013; Schwartz, 2012; Li et al., 2013; Rubin et al., 2017; Lynch et al.,
57 2016).

58 Currently, the main satellite inputs for operational aerosol modeling are AOD products
59 derived from passive-based polar orbiting imagers, such as the Moderate Resolution Imaging
60 Spectroradiometer (MODIS), the Visible Infrared Imaging Radiometer Suite (VIIRS), and the
61 Advance Very High Resolution Radiometer (AVHRR). Experimentation is proceeding with the
62 use of products from the multi-angle imaging spectroradiometer (MISR) (e.g., Lynch et al., 2016;
63 Randles et al. 2017; Buchard et al. 2017) and from geostationary instruments such as Himawari
64 and Geostationary Operational Environmental Satellite (GOES). A major advantage with such
65 passive-based satellite sensors is that the AOD is retrieved with high spatial and temporal
66 resolutions over relatively broad fields-of-view (e.g. Zhang et al., 2014). For example, MODIS
67 and VIIRS provide near-global daily daytime coverage (e.g. Levy et al., 2013; Hsu et al., 2019)
68 and GOES and Himawari are capable of retrieving AOD over North American and East Asia
69 regions at sub-hourly temporal resolution (e.g. Bessho et al., 2016).

70 To date, these traditional passive-based satellite AOD retrievals have been limited to darker
71 surfaces and relatively cloud-free conditions. The widely-used MODIS Dark Target aerosol data,
72 for instance, are available globally over only oceans and dark land surfaces (e.g. Levy et al., 2013).
73 The MISR and MODIS Deep Blue aerosol products are also available over some arid
74 environments, but are not applicable to snow and ice covered regions (e.g. Kahn et al., 2010; Hsu
75 et al., 2013). Also, none of the above-mentioned aerosol products are valid over cloudy regions.

76 In comparison to AOD, the semi-quantitative UV-based aerosol index (AI) has long been
77 used to monitor major aerosol events such as smoke plumes and dust storms, starting with the
78 Total Ozone Mapping Spectrometer (TOMS) from the late 1970s (Herman et al., 1997). AI is
79 derived using the ratio of observed UV radiances to simulated ones assuming only a clear Rayleigh
80 sky (e.g. Torres et al., 2007). AI retrievals are currently computed using observations from sensors
81 with ozone-sensitive channels. For example, the Ozone Monitoring Instrument (OMI), Ozone
82 Mapping and Profiler Suite (OMPS), TROPOspheric Monitoring Instrument (TROPOMI) and the
83 future Plankton, Aerosol, Cloud and ocean Ecosystem (PACE) mission include ozone sensitive
84 channels that can detect UV-absorbing aerosol particles, such as black carbon laden smoke or iron-
85 bearing dust, over bright surfaces, such as desert, snow and ice covered regions, and aerosol
86 plumes above clouds (e.g. Torres et al., 2012; Yu et al., 2012; Alfaro-Contreras et al., 2014; 2016).

87 To complement existing AOD assimilating systems, we have developed an AI data
88 assimilation (AI-DA) system that is capable of assimilating OMI AI over bright surfaces and
89 cloudy regions for aerosol analyses and forecasts. This study can be considered as one of the first
90 attempts for direct radiance assimilation in the UV spectrum for aerosol applications, as AI can be
91 directly computed from UV radiances and the developed OMI AI-DA system has all necessary
92 components for a typical radiance assimilation package. In time we expect our assimilation model

93 to merge with AOD or solar radiance assimilation to influence aerosol loading, height and
94 absorption (e.g., VIIRS+OMPS product; such as Lee et al. 2015). Details of the developed OMI
95 AI assimilation system are presented in the paper, which is organized as follows: Data sets used
96 in the study are summarized in Section 2; Section 3 discusses the components of the AI-DA
97 system. Section 4 provides an evaluation of the developed system; and Section 5 contains a
98 summary discussion.

99

100 **2.0 Datasets and Models**

101 Three datasets are used in this study. These are: (i) the OMI level 2 UV aerosol product
102 (OMAERUV; Torres et al., 2007), (ii) the Aerosol Robotic Network (AERONET; Holben et al.,
103 1998) AOD product, and (iii) reanalysis data from the Naval Aerosol Analysis and Prediction
104 System (NAAPS; Lynch et al., 2016), which was the first operational global aerosol mass transport
105 model available to the community. The assimilation system is based on spatial and temporal
106 variations of aerosol particles from NAAPS (Zhang et al., 2006; 2008), and the Vector LInearized
107 Discrete Ordinate Radiative Transfer (VLIDORT; Spurr, 2006) code is used to construct a forward
108 model for the AI-DA system.

109

110 **2.1 OMI aerosol product**

111 UV Aerosol Index data from the OMI level 2 version 3 UV aerosol products (OMAERUV)
112 are used in this study. The OMI instrument is on board the Aura satellite (launched in 2004) and
113 it observes the earth's atmosphere over the UV/visible spectrum with a pixel size of 13x24 km at
114 nadir for the global scan mode, and a swath of ~2600 km (Levelt et al., 2018). The daytime
115 equatorial crossing for the Aura platform is ~1:30 p.m. The dataset comprises the UV AI, viewing

116 and solar geometries, spectrally-dependent surface albedos at the 354 and 388 nm spectral
117 channels, terrain pressure, geolocations, x-track and algorithm quality flags, plus other aerosol and
118 ancillary parameters. The UV AI is designed to detect UV-absorbing aerosol particles, and is
119 based on radiance observations at 354 nm (I_{obs354}) and calculated radiance (I_{cal354}) at 354 nm for a
120 Rayleigh (no aerosol) atmosphere (e.g. Torres et al., 2007) as defined as

$$121 \quad AI = -100 \log_{10} \frac{I_{obs354}}{I_{cal354}}. \quad (1)$$

122 Unbiased, noise-reduced, quality-assured AI data are necessary for AI data assimilation.
123 This is especially important for OMI observations, due to this particular sensor suffering from the
124 well-referenced “row anomalies” issues (Torres et al., 2018). To remove pixels with row
125 anomalies, only retrievals with x-track flag values of 0 are retained. Also, abnormal AI values
126 were identified over mountain regions. Thus, retrievals with terrain/surface pressure less than 850
127 hpa are excluded in the study. Finally, only retrievals with OMI AI values larger than -2 are used.
128 Therefore, OMI observations over cloudy skies, which could have negative OMI AI values, are
129 also included.

130 Both cloud-free and above-cloud AI data satisfying these quality checks are aggregated /
131 averaged in $1 \times 1^\circ$ (Latitude/Longitude) bins. As a radiative transfer model run is applied for each
132 observation, the gridded data are used in the assimilation process in order to reduce the
133 computational burden. Averaged parameters for the gridded data include the solar and sensor
134 zenith angles, the relative azimuth angles, the spectrally-dependent surface albedos at 354 and 388
135 nm, the cloud fraction, and the AI values themselves. Additional quality assurance steps are also
136 applied during the spatial-averaging process. Isolated high AI values are removed as follows.
137 First, for a 4×4 pixel box, if the mean AI is less than 0.7 but an individual AI value is larger than
138 0.7, then that one value is removed. Second, if the standard deviation of AI values for a 3×3 pixel

139 box surrounding a pixel is larger than 0.5, that individual AI value is likewise removed. Note that
140 both approaches are essentially homogeneity tests that are used for identifying outliers. The
141 thresholds are estimated empirically through visual inspection.
142
143

144 **2.2 AERONET data**

145 Version 3 level 2 daytime, cloud-cleared and quality-assured AERONET data are used to
146 evaluate the performance of the OMI AI data assimilation in our study (Holben et al., 1998; Giles
147 et al., 2019). During daytime, AOD from AERONET instruments are derived by measuring the
148 attenuated solar radiance typically at seven wavelengths ranging from 340 to 1020 nm. In this
149 study, AERONET data are collocated with NAAPS analyses with and without OMI AI
150 assimilation. In order to collocate AERONET and NAAPS AOD data, AERONET AOD
151 values within ± 30 minutes of a given NAAPS analysis time are averaged and used as ground-based
152 AOD values for the NAAPS $1 \times 1^\circ$ (Latitude/Longitude) collocated bins. As AERONET data
153 require a cloud-free line of sight to the solar disk, the performance of OMI AI data assimilation
154 over overcast regions is not evaluated.

155

156 **2.3 NAAPS and NAAPS reanalysis data**

157 The NAAPS (<http://www.nrlmry.navy.mil/aerosol/>) model is a multi-species, three-
158 dimensional, Eulerian global transport model using operational Navy Global Environmental
159 Model (NAVGEM) as the meteorological driver (Hogan et al., 2014). NAAPS provides 6-day
160 forecasts at a 3-hour interval with a spatial resolution of $1/3^\circ$ (latitude/Longitude) and 42 vertical
161 levels on a global scale. NAAPS predicts four aerosol particle classes: anthropogenic and biogenic

162 fine particles (ABF, such as primary and secondary organic aerosols and sulfate aerosols); dust,
163 biomass burning smoke; and sea salt (Lynch et al, 2016).

164 The 2003-2018 NAAPS reanalysis version 1 (v1) (Lynch et al., 2016) is a modified version
165 of the operational NAAPS model. In this version, quality-controlled retrievals of AOD from
166 MODIS and MISR (Zhang et al., 2006; Hyer et al., 2011; Shi et al., 2014) are assimilated into
167 NAAPS through the Naval Research Laboratory Atmospheric Variation Data Assimilation
168 System-AOD system (NAVDAS-AOD; e.g., Zhang et al., 2008; Zhang et al., 2011; Zhang et al.,
169 2014). Aerosol source functions, including biomass burning, smoke and dust emissions, are tuned
170 regionally based on the AERONET data. Other aerosol processes, including dry deposition over
171 water, are also tuned based on AOD data assimilation correction fields. NOAA Climate Prediction
172 Center (CPC) MORPHing (CMORPH) precipitation data are used to constrain the wet removal
173 process within the tropics (Joyce et al., 2004). The usage of CMORPH avoids the ubiquitous
174 precipitation bias that exists in all global atmospheric models (e.g. Dai, 2006) and is proven to
175 improve aerosol wet deposition, therefore yielding better AOD (Xian et al., 2009). The reanalysis
176 agrees reasonably well with AERONET data on a global scale (Lynch et al., 2016) and also
177 reproduces AOD trends that are in a good agreement with satellite based analysis (e.g., Zhang and
178 Reid, 2010; Hsu et al., 2012). In this study, we use a free running version of NAAPS reanalysis v1
179 without AOD assimilation to provide aerosol fields every 6 hours at $1^\circ \times 1^\circ$ (Latitude/Longitude)
180 resolution.

181

182 **2.4 VLIDORT radiative transfer code**

183 VLIDORT is a linearized, multiple-scatter radiative transfer model for the simultaneous
184 generation of Stokes 4-vectors and analytically-derived Jacobians (weighting functions) of these

185 4-vectors with respect to any atmospheric or surface property (Spurr, 2006). The model uses
186 discrete-ordinate methods to solve the polarized plane-parallel RT equations in a multi-layer
187 atmosphere, plus the solution of a boundary value problem and subsequent source-function
188 integration to obtain radiation fields at any geometry and any atmospheric level. VLIDORT has a
189 “pseudo-spherical” *ansatz*: the treatment of solar-beam attenuation in a spherical-shell atmosphere
190 before scattering. Single-scattering in VLIDORT is accurate for both line-of-sight and solar-beam
191 spherical geometry. The model has a full thermal emission capability. VLIDORT has two
192 supplements, one dealing with bidirectional (non-Lambertian) reflection at the surface, and the
193 other with the inclusion of surface light sources (SIF or water-leaving radiances). Full details on
194 the VLIDORT model may be found in a recent review paper (Spurr and Christi, 2019, and
195 references to VLIDORT therein).

196 VLIDORT is used to simulate the AI in this study. Simulations at 354 and 388 nm are
197 performed both for Rayleigh atmospheres, and for scenarios with aerosol loadings (four mass-
198 mixing profiles for different aerosol types) taken from the NAAPS model. In addition to the AI,
199 Jacobian calculations are needed with respect to these aerosol profiles. Firstly, radiance Jacobians
200 with respect to these four mass-mixing profiles are computed analytically using VLIDORT’s
201 linearization facility, and secondly the associated Jacobians of AI are further derived through a
202 second VLIDORT linearization with respect to the Lambertian-equivalent reflectivity. The details
203 of this process is given in the next section

204

205 **3.0 OMI AI assimilation system**

206 The OMI assimilation system has three components: a forward model, a 3-D variational
207 assimilation system, and a post-processing system. Based on the background NAAPS 3-D aerosol

208 concentrations for dust, smoke, ABF, and sea salt aerosols, the forward model not only computes
209 the associated AI values, but also their Jacobians of AI with respect to the four aerosol mass-
210 loading profiles. The 3-D variational assimilation system is a modified 3-D AOD system (Zhang
211 et al., 2008; 2011; 2014) that computes increments for dust and smoke aerosol concentrations
212 based on OMI AI data. The post-processing system constructs a new NAAPS analysis based on
213 the background NAAPS aerosol concentrations and increments as derived from the 3-D variational
214 assimilation system. Details of the forward model and the modified NAVDAS-AOD system are
215 described in this section.

216

217 **3.1 Forward model for simulating OMI AI**

218 To construct an AI-DA system, a forward model is needed to simulate AI using aerosol
219 concentrations from NAAPS. In this study, the forward model is built around the VLIDORT
220 model, following a similar method to that suggested in Buchard et al. (2015). Here VLIDORT is
221 configured to compute OMI radiances and Jacobians as functions of the observational conditions
222 at 354 and 388 nm, using geolocation information from OMI data such as satellite zenith, solar
223 zenith and relative azimuth angles, as well as ancillary OMI data (surface albedos at 354 and 388
224 nm).

225 To convert from NAAPS mass-loading concentrations to aerosol extinction and scattering
226 profiles, we require aerosol optical properties for the four species at 354 and 388 nm, which are
227 summarized in Table 1. The optical properties of ABF (assumed to be sulfate in this study), sea
228 salt, dust and smoke aerosols, including mass extinction cross sections and single scattering
229 albedos at 354 and 388 nm are adapted from NASA's Goddard Earth Observing System version 5
230 (GEOS-5) model (e.g. Colarco et al., 2014; Buchard et al., 2015). Note that the study period is

231 July and August of 2007 over Africa, coinciding with the early biomass burning season associated
 232 with lower single scattering albedo values (Eck et al., 2013). With that in mind, we choose a quite
 233 low value of 0.85 for the single-scattering albedo value at 354nm (e.g. Eck et al., 2013; Cochrane
 234 et al., 2019). A slightly higher single scattering albedo of 0.86 is assumed at 388 nm. The slight
 235 increase in single scattering albedo from 354 to 388 nm has also been observed from Solar Spectral
 236 Flux Radiometer (SSFR) observations during the recent NASA ObseRvations of CLOUDS above
 237 Aerosols and their intERactionS (ORACLES) Campaign (Pistone et al., 2019). Scattering matrices
 238 for dust, smoke, sea salt and sulfate (to represent ABF) aerosols are based on associated expansion
 239 coefficients (e.g. Colarco et al., 2014; Buchard et al., 2015) taken from NASA’s GEOS-5 model.
 240 Also to reduce computational expenses, scalar radiative transfer calculations are performed.

241 To simulate OMI AI, the Lambertian Equivalent Reflectivity (LER) at 388 nm (R_{388}) is
 242 needed for estimating LER at 354 nm. The R_{388} is calculated from VLIDORT, based on equation
 243 2 below, adapted from Buchard et al. (2015), or

$$244 \quad R_{388} = \frac{I_{aer388}(\rho_{388}) - I_{ray388}(0)}{T + S_b(I_{aer388}(\rho_{388}) - I_{ray388}(0))} \quad . \quad (2)$$

245 $I_{ray388}(0)$ is the calculated path radiance at 388 nm assuming a Rayleigh atmosphere with surface
 246 albedo 0. T and S_b are the calculated transmittance and spherical albedo at 388 nm. $I_{aer388}(\rho_{388})$ is
 247 the computed radiance including 3-D aerosol fields from NAAPS and the 388 nm surface albedo
 248 from OMI data. In Buchard et al. (2015), an adjusting factor is applied to R_{388} by adding the
 249 difference between climatological surface albedos at 354 and 388 nm. The similar approach is
 250 also adopted in this study, as shown in their Equation 3.

$$251 \quad R'_{388} = R_{388} - (\rho_{388} - \rho_{354}) \quad . \quad (3)$$

252 Here, R'_{388} is surface albedo adjusted Lambertian Equivalent Reflectivity at 388 nm. ρ_{388} and ρ_{354}
 253 are surface albedo values at 388 and 354 nm channels that are obtained from the OMI OMAERUV
 254 data. Finally, the simulated AI (AI_{naaps}) is given by

$$255 \quad AI_{naaps} = -100 \log_{10} \frac{I_{aer354}(\rho_{354})}{I_{ray354}(R'_{388})} \quad . \quad (4)$$

256 Here, $I_{aer354}(\rho_{354})$ is the calculated radiance at 354 nm using NAAPS aerosol fields as well as the
 257 OMI-reported surface albedo at 354 nm (ρ_{354}). $I_{ray354}(R'_{388})$ is the calculated radiance assuming a
 258 Rayleigh atmosphere and the derived value of R'_{388} as surface albedo (Buchard et al., 2015).

259 The forward model-simulated OMI AI values are inter-compared with OMI AI values as
 260 shown in Figure 1 for the study region. A total of one month (01-31 July 2007) of NAAPS
 261 reanalysis data and OMI AI data were used. Note that OMI AI data over both cloud-free and
 262 cloudy skies were used. Since surface albedos included in the OMI data represent reflectivities
 263 under clear-sky situations, the albedo under cloudy sky is then computed

$$264 \quad \rho_{cld} = \rho_{ctr} * (1 - f_c) + 0.8 * f_c \quad . \quad (5)$$

265 Here, ρ_{ctr} and f_c are the clear sky surface albedo (e.g. ρ_{354} or ρ_{388}) and the cloud fraction, both
 266 quantities obtained from the OMI dataset. Clouds are assumed to be tropospheric (close to the
 267 surface) with an UV albedo of 0.8, such that this equation applies to both the 354 and 388 nm
 268 channels.

269 Figure 1a shows the spatial distribution of NAAPS AOD over Central and North Africa,
 270 using collocated NAAPS and OMI AI datasets. OMI AI data are grid-averaged in $1^\circ \times 1^\circ$
 271 (latitude/longitude) bins. Also, we focus over Africa in this paper as this area includes dust plumes
 272 over deserts and smoke plumes overlying stratus cloud decks. The Arctic is not included as
 273 additional efforts may be needed to fully understand properties of sea ice reflectivity; we leave this
 274 topic for a future paper. Only bins that have valid NAAPS and OMI AI data are used to generate

275 Figure 1. Dust plumes are visible over North Africa and the Persian Gulf, and a smoke plume from
 276 Central Africa is also evident. These UV-absorbing aerosol plumes are also captured by OMI AI,
 277 as seen in Figure 1c. Shown in Figure 1b are the simulated OMI AI using the NAAPS aerosol
 278 fields and viewing geometries and surface albedos from OMI. The simulated OMI AI shows
 279 similar patterns to those derived from OMI, especially for the dust plumes over North Africa and
 280 smoke plumes over Central Africa. An overall correlation of 0.785 is found between simulated
 281 and satellite-retrieved OMI AI values, as shown in Figure 1, suggesting the forward model is
 282 functioning reasonably as designed.

283

284 **3.2.1 Forward model for Jacobians of AI**

285 Jacobians of OMI AI with respect to aerosol mass concentrations are needed for the OMI
 286 AI assimilation system. In this study, AI Jacobians (K) are calculated from radiance Jacobians
 287 with respect to aerosol mass concentrations for four aerosol species (smoke, dust, ABF/sulfate,
 288 sea-salt) at 354 nm ($K_{354,nk} = \frac{\partial I_{aer354}}{\partial M_{nk}}$) and 388 nm ($K_{388,nk} = \frac{\partial I_{aer388}}{\partial M_{nk}}$) wavelengths. Here M_{nk}
 289 is the mass concentration for aerosol type, k , and for vertical layer, n . I_{aer354} and I_{aer388} are radiances
 290 for the 354 and 388 nm channels, respectively. $K_{354,nk}$ and $K_{388,nk}$ are the corresponding radiance
 291 Jacobians at 354 and 388 nm, respectively. AI Jacobians can then be calculated by analytic
 292 differentiation of the basic formula in Equation (1), and, after some algebra, we find the following
 293 result:

$$294 \quad \frac{\partial AI}{\partial M_{nk}} = \mathcal{A}_1 K_{354,nk}(\rho_{354}) + \mathcal{A}_2 K_{388,nk}(\rho_{388}) \quad . \quad (6)$$

295 Here, \mathcal{A}_1 and \mathcal{A}_2 are given respectively by Equations (7) and (8), as

$$296 \quad \mathcal{A}_1 = \left(-\frac{100}{I_{aer354}(\rho_{354}) \times \ln 10} \right) \quad , \text{ and} \quad (7)$$

$$\mathcal{A}_2 = \left(-\frac{100}{I_{ray354}(R_{388}R'_{388}) \times \ln 10} \right) \frac{\partial I_{ray354}(R_{388}R'_{388})}{\partial R} \left[\frac{(1-S_{388}R_{388})^2}{T_{388}} \right] \quad (8)$$

Based on these equations, radiance Jacobians with respect to aerosol particles, $K_{354,nk}$ and $K_{388,nk}$, are computed at 354 and 388 nm, respectively, using OMI-reported surface albedo values (ρ_{354} and ρ_{388}), followed by a calculation of the albedo Jacobian $\frac{\partial I_{aer354}(R_{388}R'_{388})}{\partial R}$ at 354 nm.

To check this analytic Jacobian calculation in Eqns. (6)-(8), we compute the aerosol AI Jacobians using a finite difference (FD) method. Here, the derivative of AI as a function of aerosol concentration of a species, k , in layer n , is computed using

$$\frac{\partial AI}{\partial M_{nk}} = \frac{(AI - AI')}{(C_{nk} - C'_{nk})} \quad (9)$$

Here C_{nk} and C'_{nk} are the baseline and perturbed aerosol concentrations, respectively, and AI and AI' are computed using C_{nk} and C'_{nk} , respectively.

Figure 2b shows the comparison of Jacobians of dust aerosols estimated from the analytic and the FD solutions. Dust, smoke, ABF and sea salt aerosol concentrations as a function of altitude are shown in Figure 2a. To compute FD Jacobians with respect to dust aerosols, a 10% perturbation is introduced in the dust profiles. A very close match is found between analytic and FD Jacobians. This validates the analytical solution used in the study. The analytic solution is of course much faster, as a single call to VLIDORT will deliver all necessary Jacobians at one wavelength, as compared to 97 separate calls to VLIDORT with the FD calculation (baseline; 4 species perturbations in the 24-layer atmosphere).

315

3.2 The variational OMI AI assimilation system

The OMI AI assimilation system is based on AI simulations (with Jacobians) from the forward model. Two principles underlay the assimilation procedure. First, we assume that OMI AI

319 is sensitive to UV-absorbing aerosol particles, such as NAAPS smoke and dust, or that only smoke
 320 and dust are injected high enough into the troposphere to impact AI. Therefore, innovations are
 321 limited to modifications of dust and smoke aerosol properties. For classes that do not strongly
 322 project onto AI, such as sea salt and ABF aerosols, aerosol concentrations are not modified during
 323 the process. Second, contributions of smoke/dust aerosols to AI ($AI_{\text{smoke}} / AI_{\text{dust}}$) prior to
 324 assimilation are estimated by multiplying smoke/dust aerosol concentrations from NAAPS with
 325 Jacobians of AI respective of smoke/dust aerosols. The ratio of AI innovation from smoke aerosols
 326 (ΔAI_{smoke}) to total AI innovation (ΔAI or $OMI\ AI - AI_{\text{naaps}}$) is assumed to be the ratio of AI_{smoke} to
 327 $AI_{\text{smoke}} + AI_{\text{dust}}$. The same assumption holds for dust aerosols.

328 Given these two principles, the overall design concept for the OMI AI assimilation can be
 329 expressed as

$$\begin{aligned}
 331 \quad C^a &= C^b + \\
 332 \quad &\frac{P_{\text{dust}} \mathbf{H}_{\text{dust}}^T}{\mathbf{H}_{\text{dust}}^T P_{\text{dust}} \mathbf{H}_{\text{dust}} + R} [y - H(C^b)] \times \frac{\mathbf{H}_{\text{dust}} C_{\text{dust}}^b}{\mathbf{H}_{\text{dust}} C_{\text{dust}}^b + \mathbf{H}_{\text{smk}} C_{\text{smk}}^b} + \\
 333 \quad &\frac{P_{\text{smk}} \mathbf{H}_{\text{smk}}^T}{\mathbf{H}_{\text{smk}}^T P_{\text{smk}} \mathbf{H}_{\text{smk}} + R} [y - H(C^b)] \times \frac{\mathbf{H}_{\text{smk}} C_{\text{smk}}^b}{\mathbf{H}_{\text{dust}} C_{\text{dust}}^b + \mathbf{H}_{\text{smk}} C_{\text{smk}}^b}, \quad (10)
 \end{aligned}$$

334
 335 where C^b and C^a are NAAPS aerosol concentrations for the analysis and background fields,
 336 respectively, C_{dust}^b and C_{smk}^b are background NAAPS particle mass concentrations for dust and
 337 smoke, $H(C)$ is the NAAPS forward model that links NAAPS parteleparticle mass concentrations
 338 to AI, and \mathbf{H} is defined as $\partial H(C) / \partial C$, which is the Jacobian matrix of AI with respect to aerosol
 339 concentrations. Y is the observed OMI AI, and $Y - H(C^b)$ is the innovation of AI, representing the
 340 difference between observed and modeled AI values.

341 The $\frac{\mathbf{H}_{dust}C_{dust}^b}{\mathbf{H}_{dust}C_{dust}^b + \mathbf{H}_{smk}C_{smk}^b}$ and $\frac{\mathbf{H}_{smk}C_{smk}^b}{\mathbf{H}_{dust}C_{dust}^b + \mathbf{H}_{smk}C_{smk}^b}$ terms are the fractional contribution
342 of innovation from dust and smoke aerosol, respectively. These terms are estimated using NAAPS
343 aerosol concentrations for relatively high aerosol loading cases (AOD > 0.15). For low aerosol
344 loading (AOD < 0.15) as reported from NAAPS, it is possible that NAAPS could underestimate
345 aerosol concentrations. Thus, the fractional contribution of innovations is assigned to 1 for the
346 dominant aerosol type based on a NAAPS aerosol climatology (Zhang et al., 2008). Note that the
347 term $[y-H(C^b)] \times \frac{\mathbf{H}_{dust}C_{dust}^b}{\mathbf{H}_{dust}C_{dust}^b + \mathbf{H}_{smk}C_{smk}^b}$ is in observational space. P_{dust} and P_{smk} are model error
348 ~~spatial~~ covariance matrices for dust and smoke ~~_(model space)~~ aerosols (e.g. Zhang et al., 2008;
349 2011; 2014). R is the observation-based error covariance ~~in model space~~. The
350 $\frac{P_{dust}\mathbf{H}_{dust}^T}{\mathbf{H}_{dust}^T P_{dust}\mathbf{H}_{dust} + R} [y-H(C^b)] \times \frac{\mathbf{H}_{dust}C_{dust}^b}{\mathbf{H}_{dust}C_{dust}^b + \mathbf{H}_{smk}C_{smk}^b}$ and $\frac{P_{smk}\mathbf{H}_{smk}^T}{\mathbf{H}_{smk}^T P_{smk}\mathbf{H}_{smk} + R} [y-H(C^b)] \times$
351 $\frac{\mathbf{H}_{smk}C_{smk}^b}{\mathbf{H}_{dust}C_{dust}^b + \mathbf{H}_{smk}C_{smk}^b}$ terms represent the estimated increments in model space.

352 The background error covariance matrix is constructed from modeled error variances and
353 error correlations, following the methodology in previous studies (Zhang et al., 2008; 2011). The
354 horizontal background error covariance is generated using the second-order regressive function
355 (SOAR), as shown in Equation 11 (Zhang et al., 2008), or

$$356 \quad C(x, y) = (1 + R_{xy}/L) \exp\left(-\frac{R_{xy}}{L}\right) . \quad (11)$$

357 Here, x and y are two given locations, and R_{xy} is the great circle distance. L is the averaged error
358 correlation length and is set to 200 km based on Zhang et al. (2008). Similarly, the vertical error
359 correlation between two pressure levels p_1 and p_2 is also based on the SOAR function, this time in
360 pressure space, based on Zhang et al., (2011), is

$$361 \quad C(p_1, p_2) = \left[1 + \left| \int_{p_1}^{p_2} \frac{d \ln p}{L} \right| \right] e^{-\left| \int_{p_1}^{p_2} \frac{d \ln p}{L} \right|} . \quad (12)$$

362 Here, L is a unit-less number representing vertical correlation length and is set to 0.015.

363 The horizontal error variance is based on the RMS error of aerosol concentrations, which
364 is arbitrarily set to $100 \mu\text{g}/\text{m}^3$ for near-surface dust aerosols (ground to 700 hPa). The RMS error
365 of dust aerosol mass is assumed to decrease as altitude increases, and is set to 50%, 25%, and 1%
366 of the near-surface values for 500-700, 350-500 and 70-350 hPa respectively. Note that different
367 aerosol species have different mass extinction values. Here we assume the modeled error in
368 aerosol extinction is the same for different aerosol species and thus, the RMS error of smoke
369 aerosol concentration is scaled by mass extinction cross section ratio between smoke and dust
370 aerosols. The observational errors are assumed to be non-correlated in this study (e.g. Zhang et
371 al., 2008). OMI AI values over cloud-free and cloudy skies are used in the study and therefore,
372 RMS errors of AI are required for both these situations. Note, as suggested by Yu et al. (2012),
373 for the same above cloud CALIOP AOD, variations in AI are found to be of the order of 1 for
374 cloud optical depth changing from 2 to 20. Thus, we assume the RMS error of OMI AI is 0.5 for
375 cloud-free skies, increasing linearly with cloud fraction up to a value of 1 for the 100% overcast.

376 Lastly, we assume that detectable UV absorbing aerosols have AI values larger than 0.8
377 (e.g. Torres et al., 2013). Therefore, for regions with OMI AI values larger than 0.8, UV absorbing
378 aerosol particles can both be added or removed from air columns based on innovations, which are
379 the differences between OMI reported and simulated AI values. For regions with OMI AI values
380 less than 0.8, innovations are only used to remove UV absorbing aerosol particles from air
381 columns.

382

383 **4.0 System evaluation & discussion**

384 **4.1 Evaluating the performance of the AI assimilation system over Africa**

385 Using two months of OMI data (July-August, 2007), the performance of OMI AI
386 assimilation was evaluated around the Africa region (20°S-40°N; ~~6~~10°W-~~5~~60°E). The study
387 region was chosen to examine the performance of OMI AI data assimilation over bright surfaces
388 such as the deserts of North Africa, as well as study aerosol advection over clouds, in this case
389 smoke off the west coast of Southern Africa. In this demonstration, two NAAPS runs were
390 performed for the period of July 1 to August 31, 2007, one with and one without the use of OMI
391 AI assimilation (AI-DA run). Both runs were initialized with the use of NAAPS reanalysis data
392 at 0000 UTC 1 July and do not include any other form of aerosol assimilation.

393 Figure 3a shows the true color composite from Aqua MODIS for July 28, 2007 over the
394 study region that is obtained from the NASA world view site
395 (<https://worldview.earthdata.nasa.gov/>; last accessed June 2020). Visible in the image are the dust
396 plumes from North Africa transported to the Atlantic Ocean, and smoke plumes from Central and
397 Southern Africa transported to the west coast of South Africa. As indicated by the aggregated
398 OMI AI data for 1200 UTC 28 July 2007 (Figure 3b), dust plumes from North Africa are
399 transported to the North corner of the west coast of North Africa. Smoke plumes are also visible
400 in the OMI AI plot in Southern Africa and are transported to the west coast and over the Atlantic.
401 Comparing Figure 3a and Figure 3b, smoke plumes, as identified from OMI, are also found over
402 cloudy regions as indicated from the MODIS visible imagery. Note that Figure 3b shows the OMI
403 AI data used in the assimilation process and again, AI retrievals over both cloud free and cloudy
404 conditions are included as suggested by Figure 3b.

405 Figure 3c is the 1200 UTC 28 July 2007 NAAPS AOD product from the natural run. In
406 comparison, Figure 3d shows the same situation, this time with the use of OMI AI data
407 assimilation. Comparing 3b with 3d, dust and smoke aerosol patterns as shown from OMI AI

408 resemble more closely the NAAPS AOD fields after AI assimilation. Over the northeast coast of
409 Africa, heavy aerosol plumes, as hinted at in NAAPS AOD from the natural run [\(Figure 3c\)](#), cover
410 larger spatial areas than those inferred from OMI AI data. In comparison, NAAPS AOD patterns
411 from the OMI AI data assimilation cycle closely resemble aerosol patterns as suggested from OMI
412 AI data. Also shown in Figures 3e and 3f are the simulated AI using NAAPS data from the natural
413 and OMI AI DA runs (data from Figures 3c and 3d) respectively. Clearly, with the use of NAAPS
414 data from the natural run, simulated OMI AI are overestimated in comparison with OMI AI data
415 (Figure 3b). Simulated AI patterns with the used of NAAPS data from the OMI AI DA run rather
416 closely resemble AI patterns from the OMI data, again, indicating the OMI AI DA system is
417 functioning reasonably as designed.

418 The performance of AI-DA is also evaluated using OMI AI for the whole study period, as
419 shown in Figure 4. These data are constructed using collocated OMI AI and NAAPS data
420 according to the conditions introduced in Sec. 3. Here, Figures 4a and 4e are spatial distributions
421 of two-monthly averaged (July and August 2007) AODs for NAAPS AI-DA and natural runs,
422 respectively. Figure 4b is the spatial distribution of the simulated AI using NAAPS data from AI-
423 DA runs, and Figure 4c is the spatial distribution of OMI AI for the two-month period. Figures 4f
424 and 4g show similar plots to those in Figures 4c and 4d, but this time for NAAPS natural runs.
425 While simulated AI values from NAAPS natural runs (Figure 4f) are overestimated compared to
426 OMI AI values (Figure 4g) for the study region, the patterns of simulated AI from NAAPS AI-DA
427 runs (Figure 4b) are similar to patterns shown from OMI AI (Figure 4c). This is also seen from
428 Figure 4d, which is the difference between simulated AI from NAAPS AI-DA runs and OMI AI.
429 In contrast with the situation in Figure 4d, Figure 4h, which is the difference between simulated
430 AI from NAAPS natural runs and OMI AI, shows much larger differences in AI values.

431 While it is not too difficult to make the model mimic the AI product, proof of real skill lies
432 in any improvements to AOD calculations. To this end, the performance of OMI AI assimilation
433 was evaluated with the use of AERONET data. Figure 5a shows the inter-comparison of NAAPS
434 AOD versus AERONET AOD at 0.55 μm . A total of 14~~4350~~ collocated pairs of NAAPS and
435 AERONET data were compiled for the study region over the two months test period. Comparing
436 with AERONET data, NAAPS AOD from the natural run had a correlation of 0.6~~84~~, a mean
437 absolute error in AOD of 0.1~~547~~, and an RMSE of 0.2~~205~~. In comparison, with AI assimilation,
438 NAAPS AOD correlations to AERONET increased to 0.7~~42~~ (Figure 5b), the absolute error
439 reduced to 0.1~~042~~, and RMSE reduced to 0.1~~568~~, both roughly a 30% reduction. Note that
440 AERONET AOD values are only available for lines-of-sight that are free of cloud presence for the
441 sun photometer instruments. Also, the slope of AERONET versus NAAPS AOD is 0.~~8793~~ for the
442 NAAPS natural runs, and a similar slope of 0.~~8492~~ is found for the NAAPS AI-DA runs.

443

444 **4.2 Inter-comparison with AOD data assimilation**

445 Typically, NAAPS reanalyses are constructed through assimilation of MISR and MODIS
446 aerosol products (NAAPS AOD assimilation). Thus, the performances of NAAPS AOD and AI-
447 DA assimilations are compared against AERONET data. Figure 5c shows the comparison of
448 AERONET AOD and NAAPS AOD after AOD assimilation, while Figure 5b shows a similar plot
449 but using NAAPS data from AI-DA. Note that the same version of the NAAPS model with the
450 same temporal and spatial resolutions, and driven by the same meteorological data, were used in
451 constructing Figure 5 and thus the differences in Figures 5a, 5b and 5c only result from different
452 aerosol data assimilation methods implemented (no data assimilation for the natural run). A better
453 correlation between AERONET and NAAPS data of 0.~~7982~~ ~~is and a slope of 1.01 are~~ found using
454 AOD data assimilation. In comparison, the correlation is 0.7~~42~~ ~~and the slope is 0.92~~ for the AI-

455 DA runs. Slightly better RMSE (0.1~~405~~ versus 0.1~~568~~) and absolute error (0.~~09544~~ versus 0.1~~042~~)
456 values are also found for the AOD data assimilation runs. This result is not surprising as OMI AI
457 provides only a proxy for aerosol properties while passive-based AOD retrievals are often
458 considered as a more reliable parameter for representing column-integrated aerosol properties. But
459 still, the evaluation efforts are over cloud-free line-of-sight as detected from AERONET, AI DA
460 may further assist traditional AOD data assimilation by ~~proving~~providing AI assimilation over
461 cloudy regions.

462

463 **4.3 Sensitivity test**

464 As mentioned in Section 3, aerosol properties for non-smoke aerosol types were obtained
465 from the NASA GEOS-5 model (e.g. Colarco et al., 2014; Buchard et al., 2015). Yet, different
466 smoke aerosol SSA values are used in this study, as values for central Africa have a strong seasonal
467 dependency (e.g. Eck et al., 2013). While SSA values of 0.85 and 0.86 are used for the 354 and
468 388 nm channels, respectively, in our study, we have also examined the sensitivity of simulated
469 OMI AI with respect to differing SSA values (Figure 6). Figures 6a-c show the simulated AI at
470 1200 UTC 28 July 2007 using NAAPS reanalysis data (Lynch et al, 2016) for three scenarios: SSA
471 values at 354 and 388 nm of 0.84 and 0.84 (Figure 6a), 0.85 and 0.85 (Figure 6b) and 0.86 and
472 0.86 (Figure 6c). Over the central Africa area, where smoke plumes are expected, simulated OMI
473 AI patterns are similar for Figures 6a and 6b, but reduced values in AI are found when using higher
474 SSA values of 0.86 at both 354 and 388 nm. This is further confirmed by the averaged AI for the
475 smoke region over central Africa (~~14.5-0.5°~~ to ~~-1450.5°~~ S latitude and 10.5° to 30.5° E longitude;
476 indicated using the black box in Figure 6f) of 0.96, 0.94 and 0.78 for Figures 6a, 6b and 6c
477 respectively.

478 Figures 6d-f show the sensitivity for adjustments of the SSA values at 388nm while
479 maintaining a fixed SSA value of 0.85 at 354 nm. Here the SSA values at 388 nm are set to 0.85,
480 0.855 and 0.86 for Figures 6d, 6e and 6f respectively. Interestingly, the spectral dependence of
481 SSA seems to affect the simulated AI significantly, and this phenomenon has also been reported
482 by previous studies (e.g. Hammer et al., 2017). The averaged AI values over central Africa (again,
483 indicated by the black box in Figure 6f) are 0.94, 1.11 and 1.32 for 388 nm SSAs of 0.85, 0.855
484 and 0.86, respectively. This exercise suggests that simulated AI is a strong function of SSA, so
485 that both the spectral dependence of SSA values at 354 and 388 nm and reliable SSA values are
486 needed on a regional basis for future applications.

487 Interestingly, although simulated AI values are significantly affected by perturbing SSA
488 values as shown in Figure 6, less significant impacts are observed for NAAPS AOD. This is found
489 by running the OMI AI DA for 1200UTC, July 28, 2015 for SSA values used in generating Figure
490 6. For example, for the black box highlighted region in Figure 6f, the averaged values for the
491 simulated OMI AI are 0.96, 0.94 and 0.78 for using SSA values at 354 / 388 nm channels of 0.84
492 / 0.84, 0.85 / 0.85 and 0.86 / 0.86, respectively. The corresponding NAAPS AODs are found to
493 be 0.559, 0.560 and 0.585 after OMI AI DA, which is a change of less than 5%. Similar, by fixing
494 the SSA value of the 354 nm channel as 0.85 and perturbing SSA values at 388 nm from 0.85 to
495 0.86, a ~30% change is found in simulated OMI AI (from 0.94 to 1.32), yet a ~10% change is
496 found for the NAAPS AOD (from 0.560 to 0.504) after OMI AI DA.

497 It is also of interest to investigate the changes in aerosol vertical distributions due to the
498 OMI AI DA. For this exercise, we selected the 1200 UTC 28 July 2007 case and compared vertical
499 distributions of smoke and dust aerosols near the peak AI value of the smoke plume (9.5°S and
500 20.5°E) for the NAAPS natural and AI DA runs (Figure 7a). Note that the differences between

501 OMI DA and natural runs as shown in Figure 7 are essentially an integrated effect of OMI AI DA
502 from 00Z, July 01 to 12 Z, July 28, 2007. As shown in Figure 7a, the corrections to dust and
503 smoke aerosol concentrations from the AI DA system seem to be systematic changes across the
504 majority of vertical layers, instead of moving dust or smoke aerosol plumes vertically. As dust
505 aerosol concentrations are reduced at all layers and a systematic correction to smoke aerosol
506 concentrations, although non-linear, is also observed. AI assimilation helps reduce the amount of
507 upper troposphere dust (likely to be artifact) but does change the layer centroid slightly upwards.
508 We have also evaluated NAAPS vertical distributions near a peak dust plume region (25.5°N and
509 12.5°W) for the 12Z 28 July 2007 case as shown in Figure 7b. Similar to Figure 7a, a non-linear
510 correction to dust aerosol concentrations is also observed across the vertical domain.

511

512 **4.4 Issues and discussions**

513 The OMI AI data assimilation system is a proxy for all-sky, all-band modeling system
514 radiance assimilation. It contains all the necessary components for such radiance assimilation,
515 including a forward model for simulating radiances and AI values and their Jacobians, based on a
516 full vector linearized radiative transfer model called for every observation. Therefore, the
517 computational burden is a direct issue associated with the deployment of calls to a radiative transfer
518 model for each observation. For the study area in this work, after binning OMI AI data into a
519 $1^\circ \times 1^\circ$ (Latitude/Longitude) product, it still takes about ~1 CPU day for NAAPS to run for one
520 month of model time. In comparison, the time scale for running AOD assimilation for 1 month is
521 at the hourly scale level. Clearly, there will be an unavoidable computational burden of some sort
522 for OMI AI assimilation and by extension, for future radiance assimilation in the UV/visible
523 spectrum for aerosol analyses. Performance enhancement methods, such as parallel processing

524 (the VLIDORT software is thread-safe and can be used in parallel environments such as OpenMP),
525 or fast look-up-table extraction based on neural-networks and trained data sets of forward
526 simulation, must be explored in order to enable such assimilation applications in near real time on
527 a global scale.

528 In contrast with the assimilation of retrieved aerosol properties, both aerosol absorption
529 and scattering need to be accounted for when assimilating radiance or OMI AI in the UV spectrum.
530 This requires the inclusion of more dynamic aerosol optical properties into the data assimilation
531 process, and properties that vary with region and season. As noted already, even for biomass
532 burning aerosols over South Africa, lower single scattering albedo values were found at earlier
533 stages of burning seasons (e.g. Eck et al., 2013). A look-up-table of aerosol optical properties as
534 functions of region and season will be needed for global implications of OMI AI as well as future
535 radiance assimilation for aerosol modeling.

536 OMI AI is sensitive to above-cloud UV-absorbing aerosols (e.g. Yu et al., 2012; Alfaro-
537 Contreras et al., 2014), and therefore, OMI AI values over cloudy scenes were also used in this
538 study. However, OMI AI cannot be used to infer aerosol properties for aerosol plumes beneath a
539 cloud deck. For regions with high clouds, the use of OMI AI data assimilation will likely result in
540 an underestimation of AOD as below-cloud aerosol plumes are not accounted for. Therefore, only
541 OMI AI data over low cloud scenes are to be used for aerosol assimilation efforts. In addition,
542 although some quality assurance steps were applied in this study for the OMI AI data, lower AI
543 values were observed over glint regions near the west coast of Africa. Abnormally high OMI AI
544 values are also seen near the Arctic region - this may be related to the presence of floating ice
545 sheets. Thus, innovative and detailed data screening and quality assurance steps are needed to

546 exclude potentially noisy OMI AI retrievals and for further application of OMI AI data
547 assimilation on a global scale.

548 Even with these known issues, OMI AI assimilation as presented in the study illustrates a
549 new method for assimilating non-conventional aerosol products. Bearing in mind that OMI AI
550 assimilation is essentially radiance assimilation in the UV spectrum, this study demonstrates the
551 potential of directly assimilating satellite radiance in the UV/visible spectrum for aerosol modeling
552 and analyses.

553

554 **5.0 Conclusions**

555 The OMI aerosol index (AI), which measures the differences between simulated radiances
556 over Rayleigh sky and observed radiances at 354 nm, has been used to detect the presence of
557 absorbing aerosols over both dark and bright surfaces. We have constructed a new assimilation
558 system, based on the VLIDORT radiative transfer code as the major component of the forward
559 model, for the direct assimilation of OMI AI. The aim is to improve accuracies of aerosol analyses
560 over bright surfaces such as cloudy regions and deserts.

561 The performance of the OMI AI data assimilation system was evaluated over South-Central
562 and Northern Africa regions for the period of 01 July -31 August 2007. This evaluation was done
563 through inter-comparing NAAPS analyses with and without the inclusion of OMI AI data
564 assimilation. Besides cloud-free AI retrievals over dark surfaces, OMI AI retrievals over desert
565 regions and over areas were also considered. When compared against AERONET data, a total of
566 ~298% reduction in Root-Mean-Square-Error (RMSE) with a ~32% reduction in absolute error
567 were found for NAAPS analyses with the use of OMI AI assimilation. Also, NAAPS analyses
568 with the inclusion of OMI AI data assimilation show similar aerosol patterns to those in the OMI
569 AI data sets, showing that our OMI AI data assimilation system works as expected.

570 This study also suggests that NAAPS analyses with OMI AI data assimilation cannot out-
571 perform NAAPS reanalyses data that were incorporated with MODIS and MISR AOD
572 assimilation, and validated against AERONET data. This is not surprising, as OMI AI is only a
573 proxy for the AOD and is sensitive to other factors such as surface albedo and aerosol vertical
574 distribution. Also, AERONET data are only available over cloud-free field of views, so the
575 performance of our OMI AI data assimilation system over cloudy regions has not been evaluated.

576 There are a number of issues arising from our study. For example, aerosol optical
577 properties are needed for the OMI AI-DA system - these have strong regional and temporal
578 signatures that need to be carefully quantified before applying them to the AI-DA on a global scale.
579 Also, OMI AI retrievals are rather noisy and contain known and unknown biases. Abnormally
580 high OMI AI values are found over mountain regions as well the polar regions. Sporadic high AI
581 values are also known to occur, for reasons that are still not properly understood. Even though
582 quality assurance steps were proposed in this study, detailed analysis of OMI AI data are needed
583 for future implementation of OMI AI data assimilation for aerosol studies.

584 Lastly, AI values are derived from radiances and thus, the AI-DA system presented in the
585 study can be thought of as a radiance assimilation system for the UV spectrum. This is because
586 the AI-DA system contains all necessary components for radiance assimilation, based on a forward
587 model for calculating not only simulated satellite radiances, but also the aerosol-profile Jacobians
588 of these radiance, both quantities as functions of observation conditions. This study is among the
589 first attempts at radiance assimilation at the UV spectrum and indicates the future potential for
590 direct radiance assimilation at the UV and visible spectra for aerosol analyses and forecasts.

591

592 **Author contributions.** All authors contributed to the overall design of the study. Authors JZ and
593 RS coded the system. Author JSR provided valuable suggestions though the study. Author PX
594 assist with the evaluation of the system.

595
596 **Code and data availability:** The OMI data assimilation scheme (V1.0) is constructed using
597 VLIDORT and NAVDAS-AOD for NAAPS analyses and forecasts. The VLIDORT radiative
598 transfer mode is a property of RT Solutions Inc. The VLIDORT code is publicly available, and
599 comes with a standard GNU public license, through direct contact with RT Solutions Inc.
600 (http://www.rtslidort.com/mainprod_vlidort.html). Both NAAPS and NAVDAS-AOD are
601 proprietary to Naval Research Laboratory, United States Department of the Navy. Nevertheless,
602 both NAAPS and NAVDAS-AOD are well documented in past studies (e.g. Lynch et al., 2016;
603 Zhang et al., 2008; 2011; 2014; Rubin et al., 2017) and we have made every effort to thoroughly
604 report our methods so that they may be replicated. AOD fields from the NAAPS OMI AI DA and
605 natural runs over the study region and period are shared as the supplement to the paper for readers
606 who are interested. The NAAPS reanalysis data are available from the USGODAE web site
607 (https://nrlgodae1.nrlmry.navy.mil/cgi-bin/datalist.pl?dset=nrl_naaps_reanalysis&summary=Go).
608 The OMI OMAERUV data are available from the NASA's Goddard Earth Sciences *Data and*
609 Information Services Center (*GES DISC*;
610 https://disc.gsfc.nasa.gov/datasets/OMAERUV_003/summary). AERONET data are obtained
611 from the NASA AERONET webpage (<https://aeronet.gsfc.nasa.gov/>).

612 ~~**Code and data availability:** The VLIDORT radiative transfer model is available to the public~~
613 ~~through contacting RT solutions Inc. (http://www.rtslidort.com/mainprod_vlidort.html).~~ The
614 ~~NAAPS model belongs to the Naval Research Laboratory and is not publically available. The~~

615 ~~NAAPS reanalysis data are available from the USGODAE web site~~
616 ~~(https://nrlgodae1.nrlmry.navy.mil/cgi-bin/datalist.pl?dset=nrl_naaps_reanalysis&summary=Go.~~
617 ~~The OMI-OMAERUV data are available from the NASA's Goddard Earth Sciences Data and~~
618 ~~Information Services Center (GES DISC;~~
619 ~~https://disc.gsfc.nasa.gov/datasets/OMAERUV_003/summary).~~ AERONET data are obtained
620 ~~from the NASA AERONET webpage (<https://aeronet.gsfc.nasa.gov/>).~~

621

622 **Competing interests.** The authors claim no competing interests.

623

624 **Acknowledgements.** We thank the NASA AERONET group for the sun-photometer data used in
625 the study. “We acknowledge the use of imagery from the NASA Worldview application
626 (<https://worldview.earthdata.nasa.gov>), part of the NASA Earth Observing System Data and
627 Information System (EOSDIS).”

628

629 **Financial support.** This study is supported by the NASA grant NNX17AG52G. Co-Author JSR
630 was supported by the Office of Naval Research Code 322.

631

632

633

634 **References:**

- 635 Alfaro-Contreras, R., Zhang, J., Campbell, J. R., and Reid, J. S.: Investigating the frequency and
636 trends in global above-cloud aerosol characteristics with CALIOP and OMI, *Atmos. Chem.*
637 *Phys.*, 16, 47-69, doi:10.5194/acp-16-47-2016, 2016.
- 638 Alfaro-Contreras R., Zhang, J., Campbell, J. R., Holz, R. E., and Reid, J. S.: Evaluating the Impact
639 of Aerosol Particles above Cloud on Cloud Optical Depth Retrievals from MODIS, *J.*
640 *Geophys. Res. Atmos.*, 119, 5410–5423, doi:10.1002/2013JD021270, 2014.
- 641 Benedetti, A., et al., Aerosol analysis and forecast in the European Centre for Medium-Range
642 Weather Forecasts Integrated Forecast System: 2. Data assimilation, *J. Geophys. Res.*, 114,
643 D13205, doi:10.1029/2008JD011115, 2009.
- 644 Bessho, K., Date, K., Hayashi, M., Ikeda, A., Imai, T., Inoue, H., Kumagai, Y., Miyakawa, T.,
645 Murata, H., Ohno, T., Okuyama, A., Oyama, R., Sasaki, Y., Shimazu, Y., Shimoji, K.,
646 Sumida, Y., Suzuki, M., Taniguchi, H., Tsuchiyama, H., Uesawa, D., Yokota, H., &
647 Yoshida, R.: An Introduction to Himawari-8/9- Japan's New-Generation Geostationary
648 Meteorological Satellites. *Journal of the Meteorological Society of Japan. Ser. II*, 94(2),
649 151–183. <https://doi.org/10.2151/jmsj.2016-009>, 2016.
- 650 Buchard, V., Randles, C., Silva, A., Darmenov, A., Colarco, P., Govindaraju, R., Ferrare, R., Hair,
651 J., Beyersdorf, A., Ziemba, L., Yu, H.: The MERRA-2 Aerosol Reanalysis, 1980 Onward.
652 Part II: Evaluation and Case Studies *Journal of Climate* [https://dx.doi.org/10.1175/jcli-d-](https://dx.doi.org/10.1175/jcli-d-16-0613.1)
653 [16-0613.1](https://dx.doi.org/10.1175/jcli-d-16-0613.1), 2017.
- 654 Buchard, V., da Silva, A. M., Colarco, P. R., Darmenov, A., Randles, C. A., Govindaraju, R.,
655 Torres, O., Campbell, J., and Spurr, R.: Using the OMI aerosol index and absorption

656 aerosol optical depth to evaluate the NASA MERRA Aerosol Reanalysis, *Atmos. Chem.*
657 *Phys.*, 15, 5743–5760, <https://doi.org/10.5194/acp-15-5743-2015>, 2015.

658 Cochrane, S. P., Schmidt, K. S., Chen, H., Pilewskie, P., Kittelman, S., Redemann, J., LeBlanc,
659 S., Pistone, K., Kacenelenbogen, M., Segal Rozenhaimer, M., Shinozuka, Y., Flynn, C.,
660 Platnick, S., Meyer, K., Ferrare, R., Burton, S., Hostetler, C., Howell, S., Freitag, S.,
661 Dobracki, A., and Doherty, S.: Above-cloud aerosol radiative effects based on ORACLES
662 2016 and ORACLES 2017 aircraft experiments, *Atmos. Meas. Tech.*, 12, 6505–6528,
663 <https://doi.org/10.5194/amt-12-6505-2019>, 2019.

664 Colarco, P. R., Nowottnick, E. P., Randles, C. A., Yi, B., Yang, P., Kim, K.-M., Smith, J. A. and
665 Bardeen, C. G.: Impact of radiatively interactive dust aerosols in the NASA GEOS-5
666 climate model: sensitivity to dust particle shape and refractive index. *Journal of*
667 *Geophysical Research: Atmospheres*, 119(2), 753– 786.
668 <https://doi.org/10.1002/2013JD020046>, 2014.

669 Dai, A.: Precipitation characteristics in eighteen coupled climate models. *Journal of Climate*, 19,
670 4605– 4630, 2006.

671 Eck, T. F., Holben, B. N., Reid, J. S., Mukelabai, M. M., Piketh, S. J., Torres, O., Jethva, H. T.,
672 Hyer, E. J., Ward, D. E., Dubovik, O., and Sinyuk, A.: A seasonal trend of single scattering
673 albedo in southern African biomass-burning particles: Implications for satellite products
674 and estimates of emissions for the world’s largest biomass-burning source, *J. Geophys.*
675 *Res.-Atmos.*, 118, 6414–6432, 2013.

676 Giles, D. M., Sinyuk, A., Sorokin, M. G., Schafer, J. S., Smirnov, A., Slutsker, I., Eck, T. F.,
677 Holben, B. N., Lewis, J. R., Campbell, J. R., Welton, E. J., Korkin, S. V., and Lyapustin,
678 A. I.: Advancements in the Aerosol Robotic Network (AERONET) Version 3 database –

679 automated near-real-time quality control algorithm with improved cloud screening for Sun
680 photometer aerosol optical depth (AOD) measurements, *Atmos. Meas. Tech.*, 12, 169–209,
681 <https://doi.org/10.5194/amt-12-169-2019>, 2019.

682 Hammer, M. S., Martin, R. V., van Donkelaar, A., Buchard, V., Torres, O., Ridley, D. A., and
683 Spurr, R. J. D.: Interpreting the ultraviolet aerosol index observed with the OMI satellite
684 instrument to understand absorption by organic aerosols: implications for atmospheric
685 oxidation and direct radiative effects, *Atmos. Chem. Phys.*, 16, 2507–2523,
686 <https://doi.org/10.5194/acp-16-2507-2016>, 2016.

687 Herman, J. R., Bhartia, P. K., Torres, O., Hsu, C., Seftor, C., and Celarier, E.: Global distribution
688 of UV-absorbing aerosols from Nimbus 7/TOMS data, *J. Geophys. Res.*, 102(D14),
689 16911–16922, doi:[10.1029/96JD03680](https://doi.org/10.1029/96JD03680)., 1997.

690 Holben, B. N., and coauthors: AERONET—A Federated Instrument Network and Data Archive
691 for Aerosol Characterization. *Remote Sensing of Environment*, 66(1), 1–16.
692 [https://doi.org/10.1016/S0034-4257\(98\)00031-5](https://doi.org/10.1016/S0034-4257(98)00031-5), 1998.

693 Hogan, T.F., Liu, M., Ridout, J. A., Peng, M. S., Whitcomb, T. R., Ruston, B. C., Reynolds, C. A.,
694 Eckermann, S. D., Moskaitis, J. R., Baker, N. L., McCormack, J. P., Viner, K. C., McLay,
695 J. G., Flatau, M. K., Xu, L., Chen, C., and Chang, S. W.: The Navy Global Environmental
696 Model, *Oceanography*, 27(3):116–125, <https://doi.org/10.5670/oceanog.2014.73>., 2014.

697 Hsu, N. C., Lee, J., Sayer, A. M., Kim, W., Bettenhausen, C., and Tsay, S.-C.: VIIRS Deep Blue
698 aerosol products over land: Extending the EOS long-term aerosol data records, *J. Geophys.*
699 *Res.-Atmos.*, 124, 4026–4053, <https://doi.org/10.1029/2018JD029688>, 2019.

700 Hsu, N. C., Jeong, M.-J., Bettenhausen, C., Sayer, A. M., Hansell, R., Seftor, C. S., Huang, J., and
701 Tsay S.-C.: Enhanced Deep Blue aerosol retrieval algorithm: The second generation, *J.*
702 *Geophys. Res. Atmos.*, 118, doi:10.1002/jgrd.50712, 2013.

703 Hsu, N. C., Gautam, R., Sayer, A. M., Bettenhausen, C., Li, C., Jeong, M. J., Tsay, S.-C., and
704 Holben, B. N.: Global and regional trends of aerosol optical depth over land and ocean
705 using SeaWiFS measurements from 1997 to 2010, *Atmos. Chem. Phys.*, 12, 8037–8053,
706 <https://doi.org/10.5194/acp-12-8037-2012>, 2012.

707 Hyer, E. J., Reid, J. S., and Zhang, J.: An over-land aerosol optical depth data set for data
708 assimilation by filtering, correction, and aggregation of MODIS Collection 5 optical depth
709 retrievals, *Atmos. Meas. Tech.*, 4, 379-408, doi:10.5194/amt-4-379-2011, 2011.

710 Joyce, J. R., Janowiak, E. J., Arkin, P. A., and Xie, P.: CMORPH: A method that produces global
711 precipitation estimates from passive microwave and infrared data at high spatial and
712 temporal resolution, *J. Hydrometeor.*, 5, 487-503, 2004.

713 Kahn, R. A., Gaitley, B. J., Garay, M. J., Diner, D. J., Eck, T. F., Smirnov, A. and Holben B. N.:
714 Multiangle Imaging SpectroRadiometer global aerosol product assessment by comparison
715 with the Aerosol Robotic Network, *J. Geophys. Res.*, 115, D23209,
716 doi:[10.1029/2010JD014601](https://doi.org/10.1029/2010JD014601), 2010.

717 Lee, J., Hsu, N.C., Bettenhausen, C., Sayer, A. M., Seftor, C. J., and Jeong, M.-J.: Retrieving the
718 height of smoke and dust aerosols by synergistic use of VIIRS, OMPS, and CALIOP
719 observations, *J. Geophys. Res. Atmos.*, 120, 8372–8388, doi:10.1002/2015JD023567, 2015.

720 Levelt, P. F., Joiner, J., Tamminen, J., Veefkind, J. P., Bhartia, P. K., Stein Zweers, D. C., Duncan,
721 B. N., Streets, D. G., Eskes, H., van der A, R., McLinden, C., Fioletov, V., Carn, S., de
722 Laat, J., DeLand, M., Marchenko, S., McPeters, R., Ziemke, J., Fu, D., Liu, X., Pickering,

723 K., Apituley, A., González Abad, G., Arola, A., Boersma, F., Chan Miller, C., Chance, K.,
724 de Graaf, M., Hakkarainen, J., Hassinen, S., Ialongo, I., Kleipool, Q., Krotkov, N., Li, C.,
725 Lamsal, L., Newman, P., Nowlan, C., Suleiman, R., Tilstra, L. G., Torres, O., Wang, H.,
726 and Wargan, K.: The Ozone Monitoring Instrument: overview of 14 years in space, *Atmos.*
727 *Chem. Phys.*, 18, 5699–5745, <https://doi.org/10.5194/acp-18-5699-2018>, 2018.

728 Levy, R. C., Mattoo, S., Munchak, L. A., Remer, L. A., Sayer, A. M., Patadia, F., and Hsu N. C.:
729 The Collection 6 MODIS aerosol products over land and ocean, *Atmos. Meas. Tech.*, 6,
730 2989–3034, [doi:10.5194/amt-6-2989-2013](https://doi.org/10.5194/amt-6-2989-2013), 2013.

731 Li, Z., Zang, Z., Li, Q. B., Chao, Y., Chen, D., Ye, Z., Liu, Y., and Liou, K. N.: A three-dimensional
732 variational data assimilation system for multiple aerosol species with WRF/Chem and an
733 application to PM_{2.5} prediction, *Atmos. Chem. Phys.*, 13, 4265–4278,
734 <https://doi.org/10.5194/acp-13-4265-2013>, 2013.

735 Lynch, P., Reid, J. S., Westphal, D. L., Zhang, J., Hogan, T. F., Hyer, E. J., Curtis, C. A., Hegg,
736 D. A., Shi, Y., Campbell, J. R., Rubin, J. I., Sessions, W. R., Turk, F. J., and Walker, A.
737 L.: An 11-year global gridded aerosol optical thickness reanalysis (v1.0) for atmospheric
738 and climate sciences, *Geosci. Model Dev.*, 9, 1489–1522, [https://doi.org/10.5194/gmd-9-](https://doi.org/10.5194/gmd-9-1489-2016)
739 [1489-2016](https://doi.org/10.5194/gmd-9-1489-2016), 2016.

740 Pistone, K., Redemann, J., Doherty, S., Zuidema, P., Burton, S., Cairns, B., Cochrane, S., Ferrare,
741 R., Flynn, C., Freitag, S., Howell, S. G., Kacenelenbogen, M., LeBlanc, S., Liu, X.,
742 Schmidt, K. S., Sedlacek III, A. J., Segal-Rozenhaimer, M., Shinozuka, Y., Stamnes, S.,
743 van Diedenhoven, B., Van Harten, G., and Xu, F.: Intercomparison of biomass burning
744 aerosol optical properties from in situ and remote-sensing instruments in ORACLES-2016,
745 *Atmos. Chem. Phys.*, 19, 9181–9208, <https://doi.org/10.5194/acp-19-9181-2019>, 2019.

746 Randles, C., Silva, A., Buchard, V., Colarco, P., Darmenov, A., Govindaraju, R., Smirnov, A.,
747 Holben, B., Ferrare, R., Hair, J., Shinozuka, Y., Flynn, C.: The MERRA-2 Aerosol
748 Reanalysis, 1980 Onward. Part I: System Description and Data Assimilation Evaluation,
749 Journal of Climate <https://dx.doi.org/10.1175/jcli-d-16-0609.1>, 2017.

750 Reid, J. S., Hyer, E. J., Prins, E. M., Westphal, D. L., Zhang, J., Wang, J., Christopher, S. A.,
751 Curtis, C. A., Schmidt, C. C., Eleuterio, D. P., Richardson, K. A., and Hoffman, J. P.:
752 Global monitoring and forecasting of biomass-burning smoke: Description and lessons
753 from the Fire Locating and Modeling of Burning Emissions (FLAMBE) program, IEEE J.
754 Sel. Top. Appl., 2, 144–162, 2009.

755 Rubin J. I., Reid, J. S., Hansen, J. A., Anderson, J. L., Holben, B. N., Lynch, P., Westphal, D. L.,
756 and Zhang, J.: Assimilation of AERONET and MODIS AOT observations using
757 Variational and Ensemble Data Assimilation Methods and Its Impact on Aerosol
758 Forecasting Skill, J. Geophys. Res., DOI: 10.1002/2016JD026067, 2017.

759 Saide, P. E., Carmichael, G. R., Liu, Z., Schwartz, C. S., Lin, H. C., da Silva, A. M., and Hyer, E.:
760 Aerosol optical depth assimilation for a size-resolved sectional model: impacts of
761 observationally constrained, multi-wavelength and fine mode retrievals on regional scale
762 analyses and forecasts, Atmos. Chem. Phys., 13, 10425–10444,
763 <https://doi.org/10.5194/acp-13-10425-2013>, 2013.

764 Schutgens, N. A. J., Miyoshi, T., Takemura, T., and Nakajima, T.: Applying an ensemble Kalman
765 filter to the assimilation of AERONET observations in a global aerosol transport model,
766 Atmos. Chem. Phys., 10, 2561–2576, <https://doi.org/10.5194/acp-10-2561-2010>, 2010.

767 Schwartz, C. S., Liu, Z., Lin, H.-C., and McKeen, S. A.: Simultaneous three-dimensional
768 variational assimilation of surface fine particulate matter and MODIS aerosol optical depth,
769 *J. Geophys. Res.*, 117, D13202, doi:10.1029/2011JD017383, 2012.

770 Sekiyama, T. T., Tanaka, T. Y., Shimizu, A., and Miyoshi, T.: Data assimilation of CALIPSO
771 aerosol observations, *Atmos. Chem. Phys.*, 10, 39–49, [https://doi.org/10.5194/acp-10-39-](https://doi.org/10.5194/acp-10-39-2010)
772 2010, 2010.

773 Sessions, W. R., Reid, J. S., Benedetti, A., Colarco, P. R., da Silva, A., Lu, S., Sekiyama, T.,
774 Tanaka, T. Y., Baldasano, J. M., Basart, S., Brooks, M. E., Eck, T. F., Iredell, M., Hansen,
775 J. A., Jorba, O. C., Juang, H.-M. H., Lynch, P., Morcrette, J.-J., Moorthi, S., Mulcahy, J.,
776 Pradhan, Y., Razinger, M., Sampson, C. B., Wang, J., and Westphal, D. L.: Development
777 towards a global operational aerosol consensus: basic climatological characteristics of the
778 International Cooperative for Aerosol Prediction Multi-Model Ensemble (ICAP-MME),
779 *Atmos. Chem. Phys.*, 15, 335–362, <https://doi.org/10.5194/acp-15-335-2015>, 2015.

780 Shi Y., Zhang J., J.S. Reid, B. Liu, E.J. Hyer, Critical evaluation of cloud contamination in the
781 MISR aerosol products using MODIS cloud masking products, *Atmos. Meas. Tech.*, 7,
782 1791-1801, doi:10.5194/amt-7-1791-2014, 2014.

783 Spurr, R. J. D., and Christi. M.: The LIDORT and VLIDORT Linearized Scalar and Vector
784 Discrete Ordinate Radiative Transfer Models: An Update for the last 10 Years, *Light*
785 *Scattering Reviews*, Volume 12, ed. A. Kokhanovsky, Springer, 2019.

786 Spurr, R. J. D.: VLIDORT: A linearized pseudo-spherical vector discrete ordinate radiative
787 transfer code for forward model and retrieval studies in multilayer multiple scattering
788 media, *J. Quant. Spectrosc. Radiat. Transfer*, 102(2), 316-342,
789 doi:10.1016/j.jqsrt.2006.05.005, 2006.

790 Torres, O., Bhartia, P. K., Jethva, H., and Ahn, C.: Impact of the ozone monitoring instrument row
791 anomaly on the long-term record of aerosol products, *Atmos. Meas. Tech.*, 11, 2701–2715,
792 <https://doi.org/10.5194/amt-11-2701-2018>, 2018.

793 Torres, O., Ahn, C., and Chen, Z.: Improvements to the OMI near-UV aerosol algorithm using A-
794 train CALIOP and AIRS observations, *Atmos. Meas. Tech.*, 6, 3257–3270,
795 <https://doi.org/10.5194/amt-6-3257-2013>, 2013.

796 Torres, O., Jethva, H., and Bhartia, P. K.: Retrieval of Aerosol Optical Depth above Clouds from
797 OMI Observations: Sensitivity Analysis and Case Studies. *J. Atmos. Sci.*, 69, 1037–1053,
798 <https://doi.org/10.1175/JAS-D-11-0130.1>, 2012.

799 Torres, O., Tanskanen, A., Veihelmann, B., Ahn, C., Braak, R., Bhartia, P. K., Veefkind, P., Levelt,
800 P.: Aerosols and surface UV products from Ozone Monitoring Instrument observations:
801 An overview. *Journal of Geophysical Research*, 112, D24S47.
802 <https://doi.org/10.1029/2007JD008809>, 2007.

803 Uno, I., Yumimoto, K., Shimizu, A., Hara, Y., Sugimoto, N., Wang, Z., Liu, Z., and Winker D.
804 M.: 3D structure of Asian dust transport revealed by CALIPSO lidar and a 4DVAR dust
805 model, *Geophys. Res. Lett.*, 35, L06803, doi:10.1029/2007GL032329, 2008.

806 Westphal, D. L., Toon, O. B., and Carlson, T. N.: A case study of mobilization and transport of
807 Saharan dust. *J. Atmos. Sci.*, 45, 2145-2175, 1988.

808 Witek M. L., Flatau, P. J., Quinn, P. K., Westphal, D. L., Global sea-salt modeling: results and
809 validation against multicampaign shipboard measurements, *J. Geophys. Res.*, 112, p.
810 D08215, [10.1029/2006JD007779](https://doi.org/10.1029/2006JD007779), 2007.

811 Xian, P., Reid, J.S., Turk, J.F., Hyer, E.J. and Westphal, D.L.: Impact of modeled versus satellite
812 measured tropical precipitation on regional smoke optical thickness in an aerosol transport

813 model, Geophysical Research Letters, 36, L16805,
814 <https://doi.org/10.1029/2009GL038823>, 2009.

815 Yu, H., Zhang Y., Chin M., Liu Z., Omar A., Remer L. A. Yang Y., Yuan T. and Zhang J.: An
816 Integrated Analysis of Aerosol above Clouds from A-Train Multi-sensor Measurements,
817 Remote Sens. Environ., 121, 125–131, <https://doi.org/10.1016/j.rse.2012.01.011>, 2012.

818 Yumimoto, K., Uno, I., Sugimoto, N., Shimizu, A., Liu, Z., and Winker, D. M.: Adjoint inversion
819 modeling of Asian dust emission using lidar observations, Atmos. Chem. Phys., 8, 2869–
820 2884, <https://doi.org/10.5194/acp-8-2869-2008>, 2008.

821 Zhang J., Reid, J. S., Campbell, J. R., Hyer, E. J., and Westphal, D. L.: Evaluating the Impact of
822 Multi-Sensor Data Assimilation on A Global Aerosol Particle Transport Model. J.
823 Geophys. Res. Atmos., 119, 4674–4689, doi:[10.1002/2013JD020975](https://doi.org/10.1002/2013JD020975), 2014.

824 Zhang, J., Campbell, J. R., Reid, J. S., Westphal, D. L., Baker, N. L., Campbell, W. F., and Hyer,
825 E. J.: Evaluating the impact of assimilating CALIOP-derived aerosol extinction profiles on
826 a global mass transport model, Geophys. Res. Lett., Vo. 38, No. 14, L14801, doi:
827 [10.1029/2011GL04773](https://doi.org/10.1029/2011GL04773), 2011.

828 Zhang, J. and Reid, J. S.: A decadal regional and global trend analysis of the aerosol optical depth
829 using a data-assimilation grade over-water MODIS and Level 2 MISR aerosol products,
830 Atmos. Chem. Phys. Discuss., 10, 18879-18917, doi:[10.5194/acpd-10-18879-2010](https://doi.org/10.5194/acpd-10-18879-2010), 2010.

831 Zhang, J., Reid, J. S., Westphal, D. L., Baker, N. L., and Hyer, E. J.: A system for operational
832 aerosol optical depth data assimilation over global oceans, J. Geophys. Res., 113, No. D10,
833 D10208, doi: [10.1029/2007JD009065](https://doi.org/10.1029/2007JD009065), 2008.

834 Zhang, J. and Reid., J.S.: MODIS Aerosol Product Analysis for Data Assimilation: Assessment
835 of Level 2 Aerosol Optical Thickness Retrievals, J. Geophysical Research-Atmospheres,
836 VOL. 111, D22207, doi:10.1029/2005JD006898, 2006.

837

838

839 Table 1. Mass extinction cross-sections (σ , m^2/g) and single scattering albedos (ω_0) used in
 840 this study.

	ABF	Dust	Smoke	Sea Salt
σ (354 nm)	7.81	0.56	6.91	0.52
ω_0 (354 nm)	1.0	0.88	0.85	1.0
σ (388 nm)	6.96	0.58	6.07	0.52
ω_0 (388 nm)	1.0	0.91	0.86	1.0

841

842

843 **Figure Captions**

844
845 **Figure 1.** (a) Spatial distribution of NAAPS AODs, using NAAPS reanalysis data from the
846 collocated OMI and NAAPS dataset for July 2007. (b). Simulated AI using NAAPS reanalysis
847 data as shown in (a). (c). Spatial distribution of OMI AI using gridded OMI data from the
848 collocated OMI and NAAPS dataset for July 2007. Grey color highlights those $1 \times 1^\circ$
849 (Latitude/Longitude) bins that have less than ~~three~~ collocated NAAPS and OMI AI data for the
850 study period.

851 **Figure 2.** (a). Vertical distributions of smoke, dust, anthropogenic and sea salt aerosols for the test
852 case as shown in (b). (b) Scatter plot of Jacobians of AI as a function of dust concentration: analytic
853 versus finite difference solutions.

854 **Figure 3.** (a). Aqua MODIS true-color image over Central and North Africa for July 28, 2007.
855 This composite was obtained from the NASA worldview site
856 (<https://worldview.earthdata.nasa.gov/>). (b). Spatial distribution of Gridded OMI AI for 12 UTC,
857 July 28, 2007. (c). Spatial distribution of NAAPS AOD from the NAAPS natural run for 12 UTC,
858 July 28, 2007. (d). Similar to (c) but using NAAPS AOD from the AI-DA run. (e). Simulated AI
859 using data from (c). (f). Simulated AI using data from (d).

860 **Figure 4.** (a). Spatial distribution of NAAPS AOD using NAAPS data from the AI-DA runs for
861 July and August 2007. Only NAAPS data that have collocated OMI AI data are used. (b). Spatial
862 distribution of simulated AI for July and August 2007 using NAAPS data from the AI-DA runs.
863 (c). Spatial distribution of gridded OMI AI for July and August 2007. (d). Differences between
864 Figures 4(b) and 4(c). (e-h) Similar to Figures 4(a)-4(d) but using NAAPS natural runs. Grey
865 color highlights those $1 \times 1^\circ$ (Latitude/Longitude) bins that have less than ~~three~~ collocated
866 NAAPS and OMI AI data for the study period.

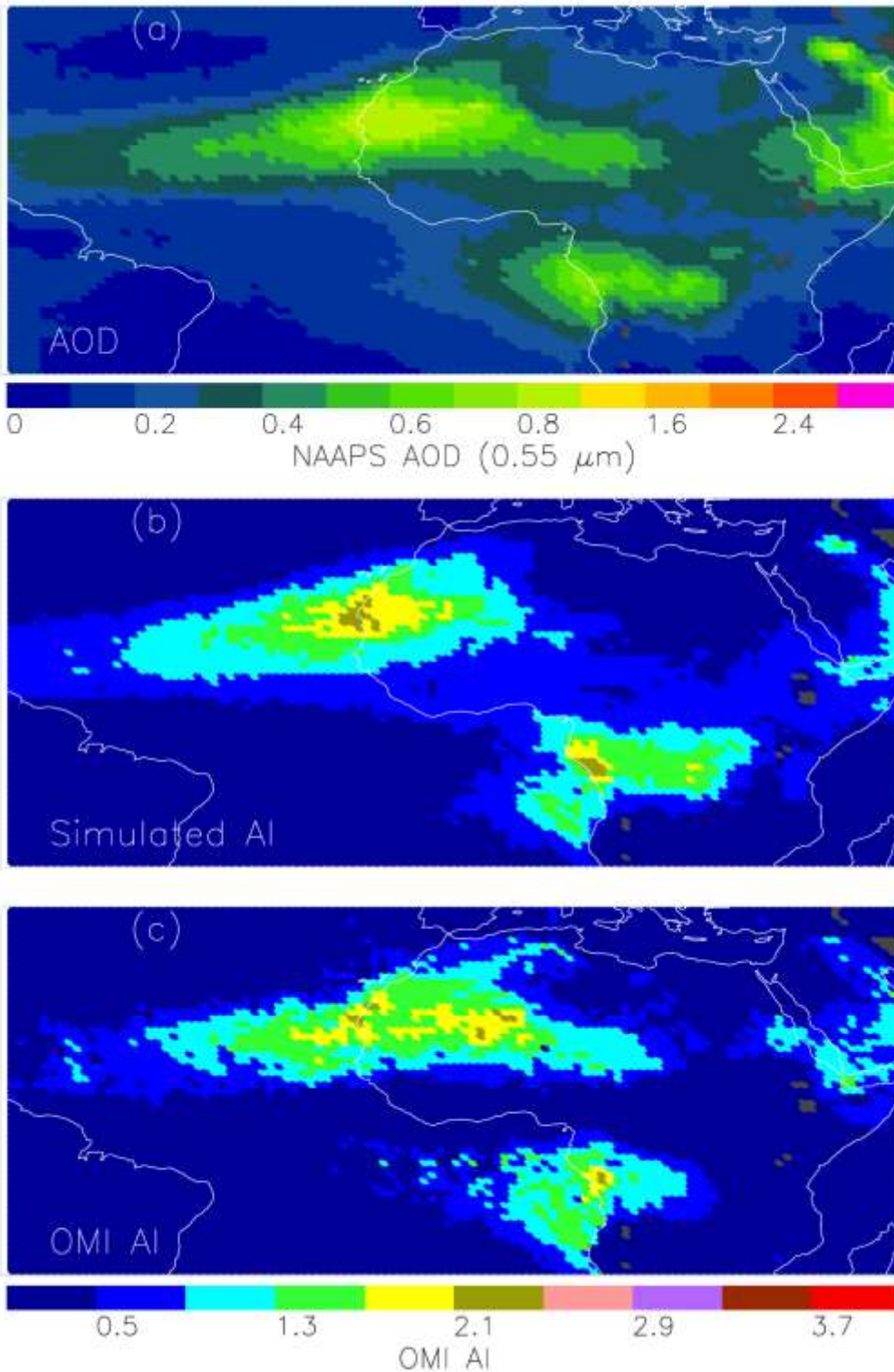
867 **Figure 5.** (a). Scatter plot of AERONET and NAAPS AOD ($0.55 \mu\text{m}$) using NAAPS data from
868 the natural runs for July-August 2007 over the study region. (b). Similar to Figure 5(a) but using
869 NAAPS data from the AI-DA runs. (c). Similar to Figure 5(a) but with AODs taken from the
870 NAAPS reanalysis.

871 **Figure 6.** Spatial distributions of simulated AI at 12 Z on July 28, 2007 using NAAPS reanalysis
872 data, with single scattering albedos of smoke aerosol at 354 and 388 nm taken to be: (a) 0.84 and
873 0.84; (b) 0.85 and 0.85; (c) 0.86 and 0.86; (d) 0.85 and 0.85; (e) 0.85, 0.855; (f) 0.85 and 0.86.

874 **Figure 7.** (a). Vertical distributions of smoke and dust aerosol concentrations over 9.5°S and
875 10.5°E at 12 Z on July 28, 2007 for both natural and AI DA runs. (b). Similar as (a) but over
876 25.5°N and 12.5°W .

877

878



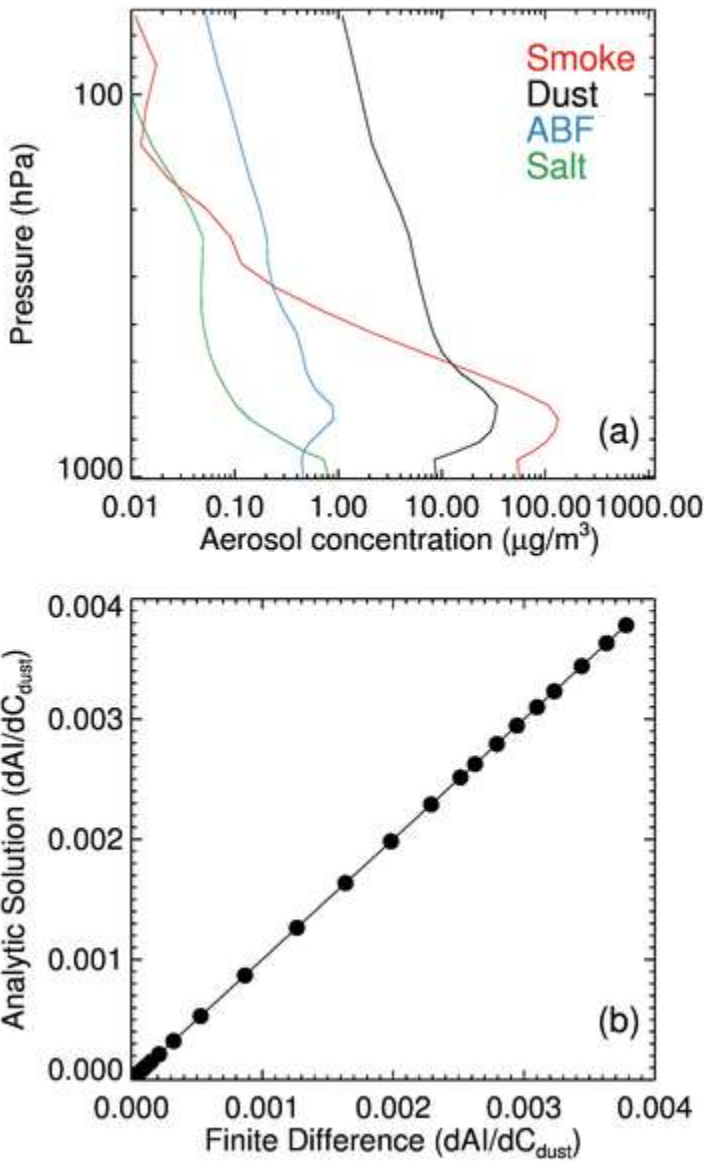
879

880

881

Figure 1. (a) Spatial distribution of NAAPS AODs, using NAAPS reanalysis data from the collocated OMI and NAAPS dataset for July 2007. (b). Simulated AI using NAAPS reanalysis data as shown in (a). (c). Spatial distribution of OMI AI using gridded OMI data from the collocated OMI and NAAPS dataset for July 2007. Grey color highlights those 1x1° (Latitude/Longitude) bins that have less than three collocated NAAPS and OMI AI data for the study period.

882



883

884 **Figure 2.** (a). Vertical distributions of smoke, dust, anthropogenic and sea salt aerosols for the test
885 case as shown in (b). (b) Scatter plot of Jacobians of AI as a function of dust concentration: analytic
886 versus finite difference solutions.

887

888

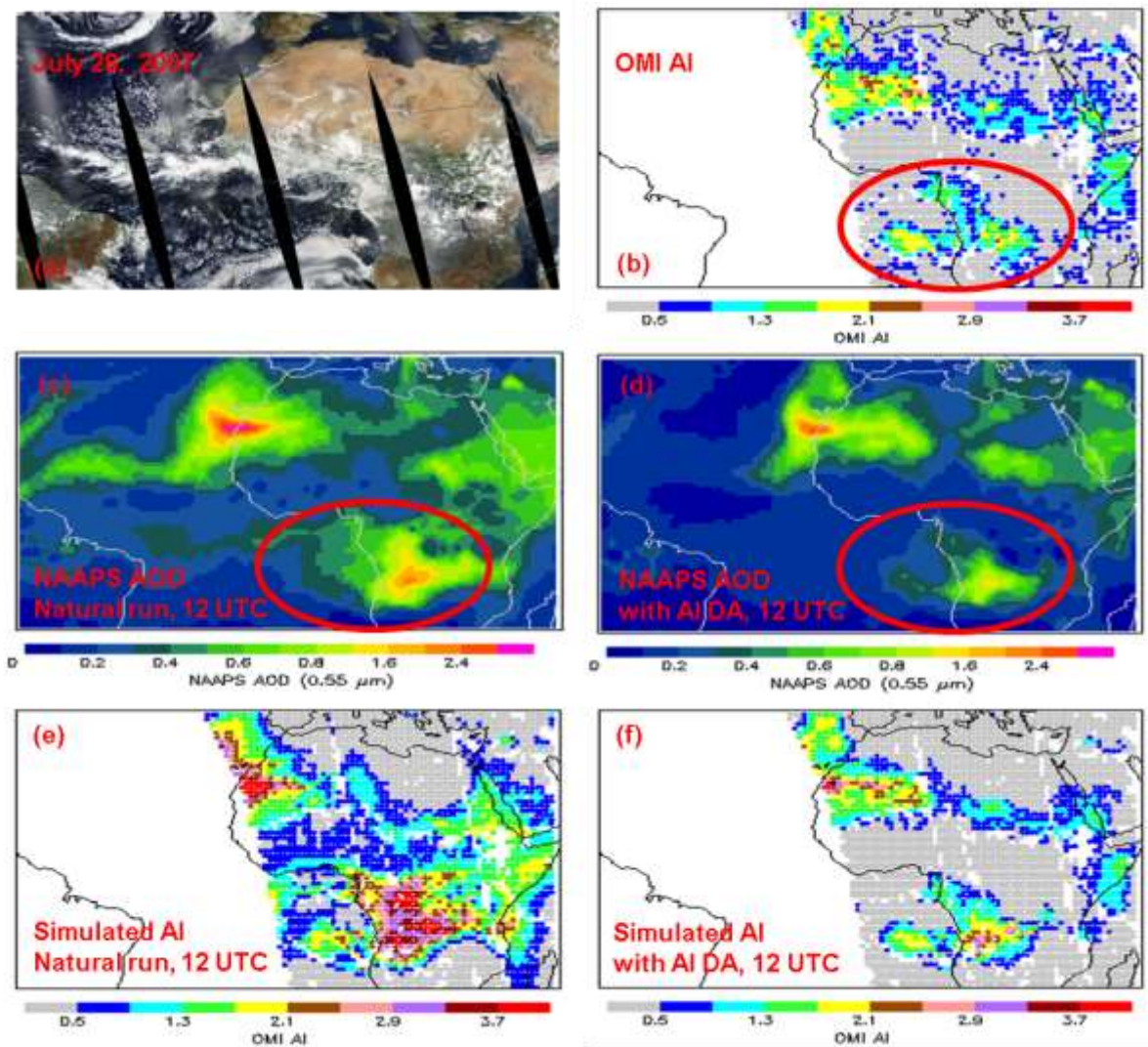
889

890

891

892

893



894

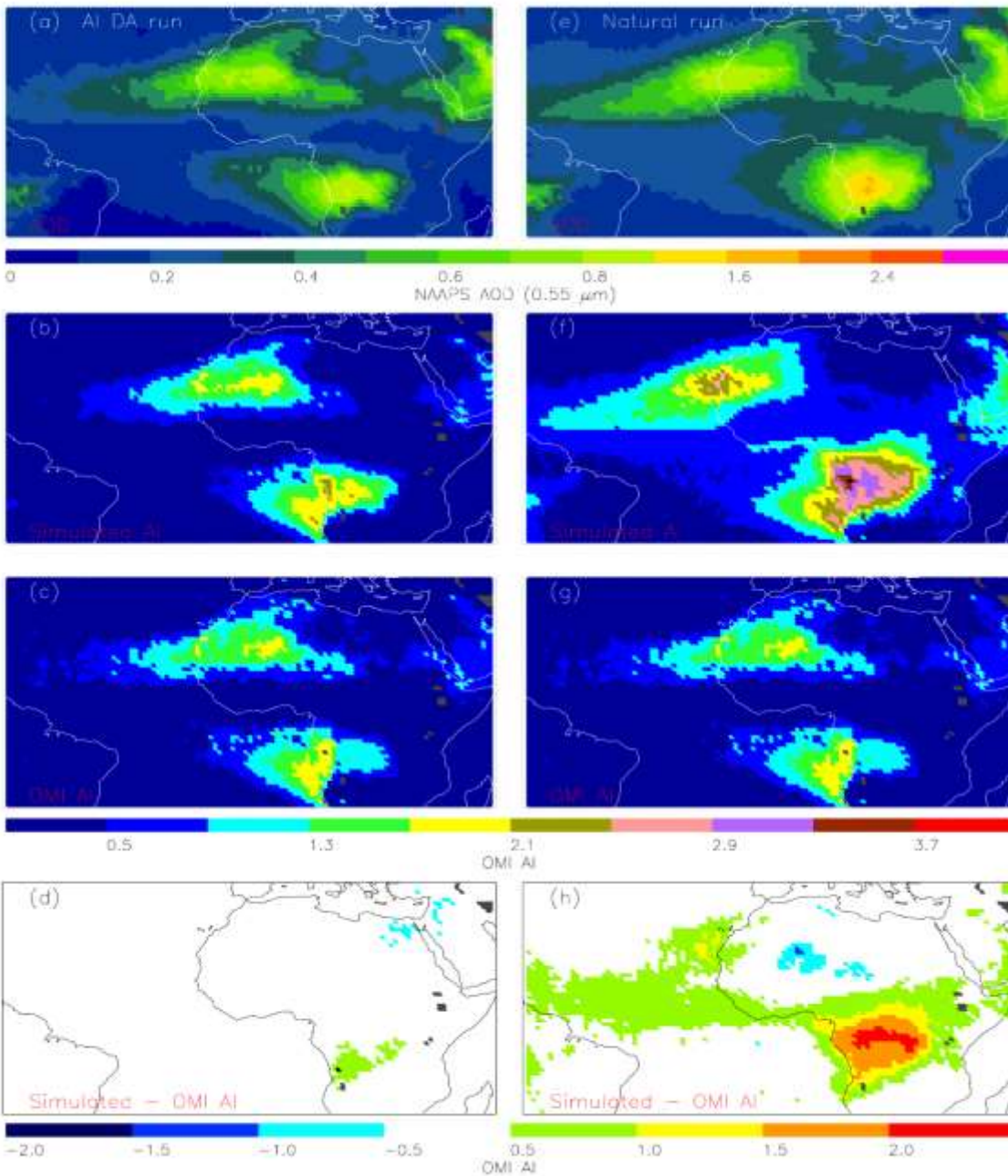
895 **Figure 3.** (a). Aqua MODIS true-color image over Central and North Africa for July 28, 2007.
896 This composite was obtained from the NASA worldview site
897 (<https://worldview.earthdata.nasa.gov/>). (b). Spatial distribution of Gridded OMI AI for 12 UTC,
898 July 28, 2007. (c). Spatial distribution of NAAPS AOD from the NAAPS natural run for 12 UTC,
899 July 28, 2007. (d). Similar to (c) but using NAAPS AOD from the AI-DA run. (e). Simulated AI
900 using data from (c). (f). Simulated AI using data from (d).

901

902

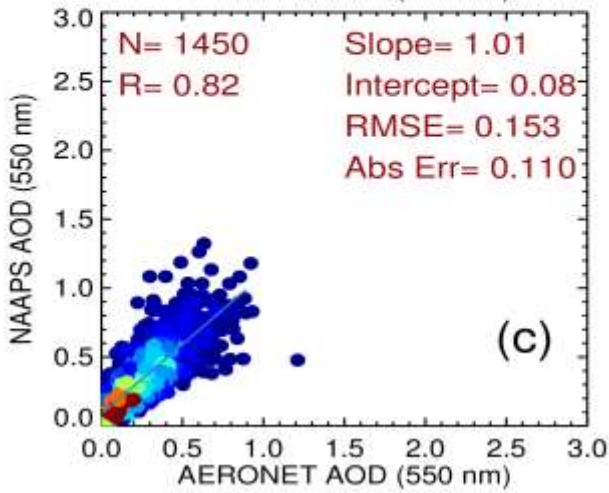
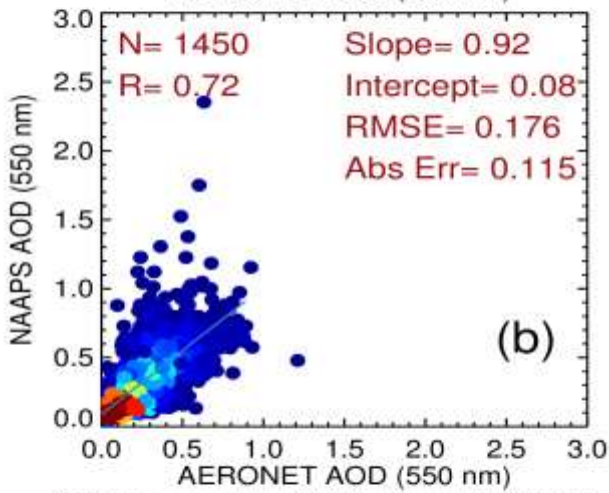
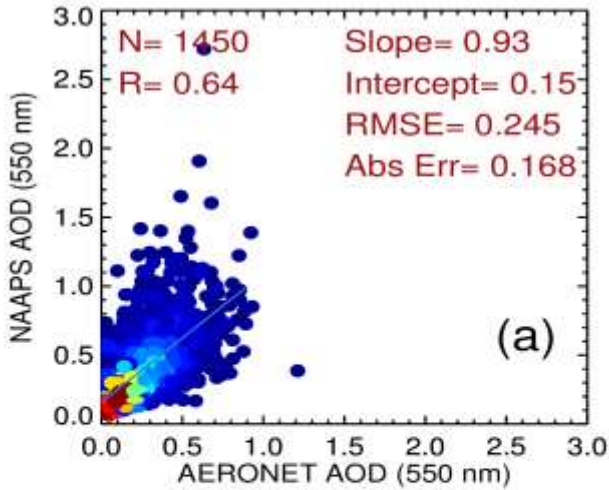
903

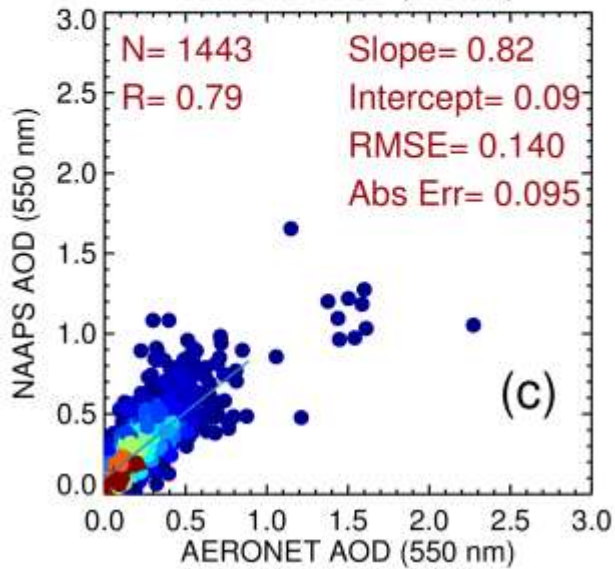
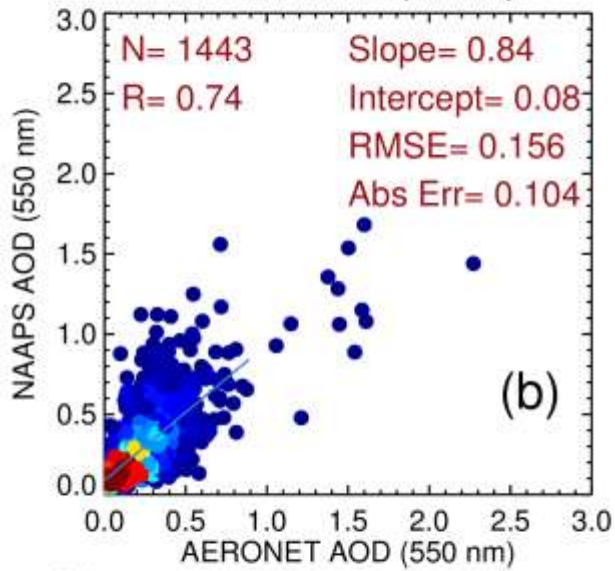
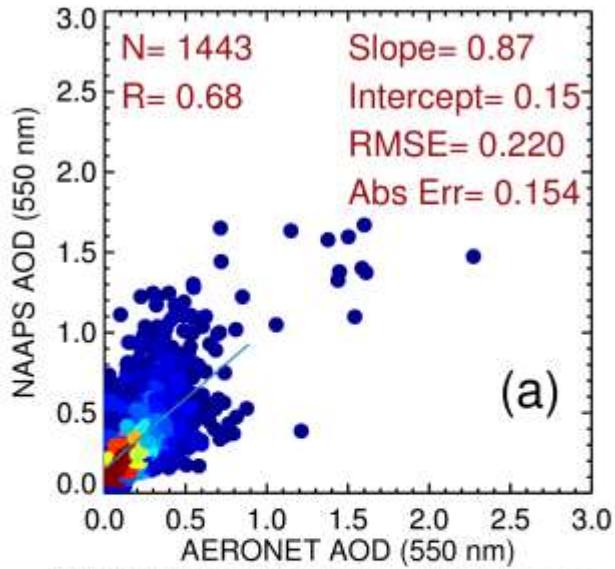
904



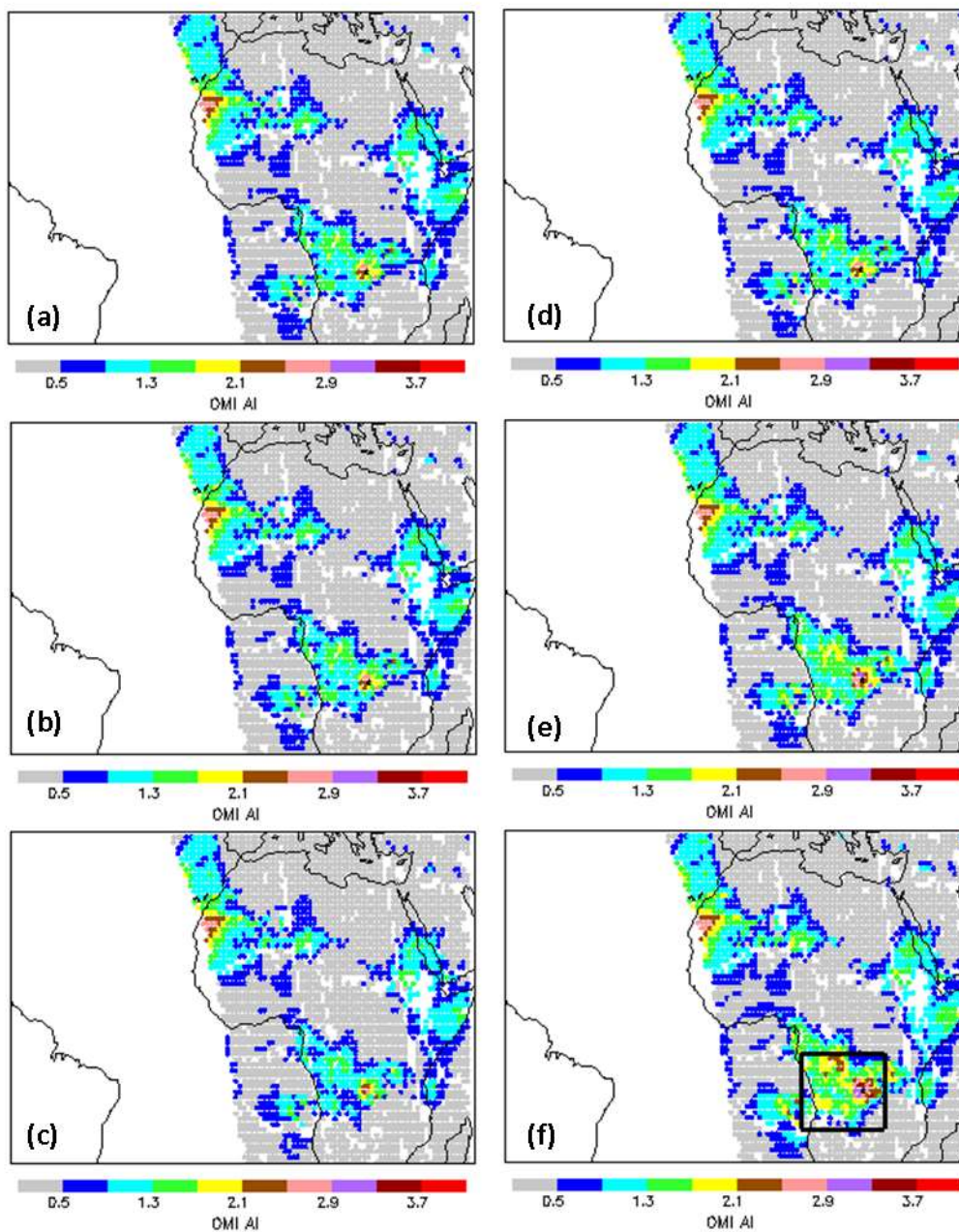
905

906 **Figure 4.** (a). Spatial distribution of NAAPS AOD using NAAPS data from the AI-DA runs for
 907 July and August 2007. Only NAAPS data that have collocated OMI AI data are used. (b). Spatial
 908 distribution of simulated AI for July and August 2007 using NAAPS data from the AI-DA runs.
 909 (c). Spatial distribution of gridded OMI AI for July and August 2007. (d). Differences between
 910 Figures 4(b) and 4(c). (e-h) Similar to Figures 4(a)-4(d) but using NAAPS natural runs. Grey
 911 color highlights those $1 \times 1^\circ$ (Latitude/Longitude) bins that have less than ~~three~~ collocated
 912 NAAPS and OMI AI data for the study period.
 913

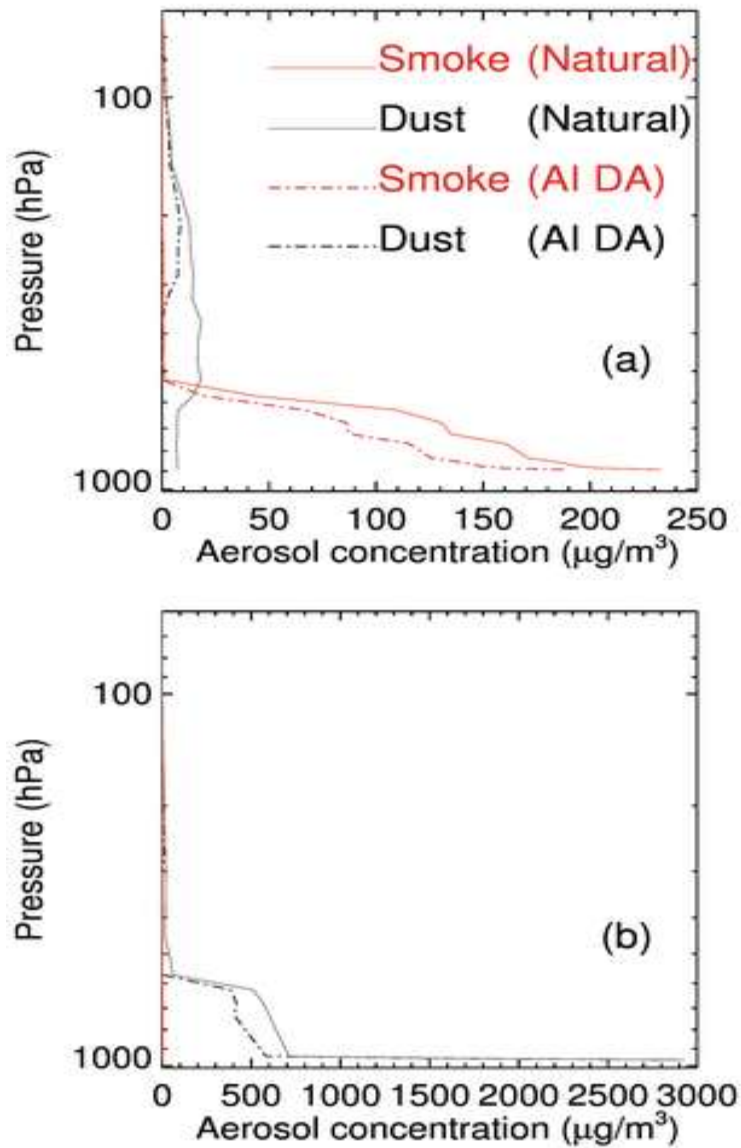




916 **Figure 5.** (a). Scatter plot of AERONET and NAAPS AOD ($0.55 \mu\text{m}$) using NAAPS data from
 917 the natural runs for July-August 2007 over the study region. (b). Similar to Figure 5(a) but using
 918 NAAPS data from the AI-DA runs. (c). Similar to Figure 5(a) but with AODs taken from the
 919 NAAPS reanalysis.
 920



921
 922 **Figure 6.** Spatial distributions of simulated AI at 12 Z on July 28, 2007 using NAAPS reanalysis
 923 data, with single scattering albedos of smoke aerosol at 354 and 388 nm taken to be: (a) 0.84 and
 924 0.84; (b) 0.85 and 0.85; (c) 0.86 and 0.86; (d) 0.85 and 0.85; (e) 0.85, 0.855; (f) 0.85 and 0.86.
 925



926

927 **Figure 7.** (a). Vertical distributions of smoke and dust aerosol concentrations over 9.5°S and
 928 10.5°E at 12 Z on July 28, 2007 for both natural and AI DA runs. (b). Similar as (a) but over
 929 25.5°N and 12.5°W.

930

931